Single Atom Catalysts (SAC) Trapped
in Defective and Nitrogen-doped Graphene Supported on Metal Substrates

Anu Baby, Laura Trovato, and Cristiana Di Valentin*

Dipartimento di Scienza dei Materiali, Università degli Studi di Milano-Bicocca,
Via Roberto Cozzi 55, 20125 Milano, Italia

Abstract

Single Atom Catalysts (SAC) in graphene have been recently gaining more and more attention. They are usually non-noble transition metal (TM) adatoms getting trapped at the carbon vacancies during the fabrication of the graphene layer, which then act as active centers for catalysis and adsorption. In this work we present a systematic and comparative investigation, by means of dispersion–corrected density functional theory (DFT) calculations, of Fe, Co, Ni, and Cu as possible SACs when they become trapped at graphene C vacancies. The stability of these TM atoms is further increased by introducing pyridinic nitrogen (N) atoms and transforming graphene into a giant porphyrin-like macrocyclic ligand. The structural, electronic and energetics properties of these systems, even under the effect of a metal substrate (weakly interacting Cu (111) or strongly interacting Ni (111)), are comparatively examined in great detail by means of crystal/ligand field theories and through ad-hoc energy decomposition analysis to highlight trends and peculiar behaviors. The position of the TM d-orbitals with respect to the Fermi level of the whole system is of considerable importance for designing prospective device applications in catalysis, electrocatalysis and sensors. To this purpose, we also examine how the reactivity of the SACs in graphene towards the hydrogen evolution reaction (HER) can be tuned with N-doping and with different substrates.

Keywords
Graphene, Nitrogen-doped, Single atom catalysts, metal substrate, transition metal atoms, HER

* Corresponding author. Tel: +390264485235 E-mail: cristiana.divalentin@unimib.it

1. Introduction

Graphene has proven to be a corrosion-protector of metal electrodes even better than the conventional anti-corrosion coatings.[1,2] The impermeability of graphene to ions as well to all kinds of gases (with the unique exception of hydrogen) has been indisputably demonstrated.[3-6] This is of paramount importance for the applications in the field of electrochemistry as such reactions usually take place in harsh corrosion prone conditions, such as in the presence of an electrolyte.[7] Until now the most successfully used electrode material has been the very expensive platinum (Pt). However, if one needs to replace it with cheaper metals, such as copper (Cu) or nickel (Ni), protecting them from corroding away in the electrolyte is fundamental and it is here that graphene would play a pivotal role.[8] Still the long-term duration of such an anti-corrosion layer under wet conditions is subject to discussion.[9]

Once the metal electrode is covered with a layer of graphene and the protection is guaranteed, the next question that arises is about reactivity. The metal beneath is now unexposed and at the surface we have pristine graphene that is not very electrochemically active.[10] But the electronic and structural properties of graphene can be suitably varied depending on the substrate on which it is grown and the fabrication methods used.[11-13] On a variety of metal substrates, such as Cu(111), Pt(111) etc., graphene is weakly interacting and hence retains its intrinsic properties, whereas on others, such as Co(111) or Ni(111), even the characteristic Dirac cone is lost due to the very strong interaction.[11] Hence, the choice of a specific substrate is a fundamental decision to make, especially in mass-production.

Recently there has been a lot of effort and interest in a new area of research that is capable of instigating additional attributes to the existing characteristics of graphene by introducing dopant heteroatoms in the 2D hexagonal matrix.[14] A quite interesting response towards the electrochemical activity has been reported on the non-noble metal atoms getting trapped at carbon vacancies and defects, the so-called Single Atom Catalysts (SAC) in a graphene layer.[15-17] These SACs could be either metal adatoms originating from the substrate and getting trapped in graphene during the growth process or purposefully incorporated by means of sputtering.[18] However, it may happen that the bonds formed between the C atoms of graphene and the SAC are not very stable in the catalytic conditions. A solution to this problem is interposing N atoms, which increases the binding strength between the non-noble metal atom and graphene. Furthermore, the presence of N has proven to reduce the activation

barrier of the reaction at SAC, conceding it to proceed at room temperature.[19] It has been shown that N doping reduces the overpotential for the hydrogen evolution reaction (HER) at the SAC sites on graphene.[20] Similarly an increased catalytic activity towards ORR and H_2O_2 reduction has also been reported in the presence of N atoms.[21,22] Fabrication of such structures have been successfully done by introducing the N atoms in the graphene matrix by CVD employing N containing molecules as precursors, or first sputtering graphene followed by thermal treatment with N containing precursors, or very recently from a N-doped nickel substrate.[23-26] Hence, by combining metal and non-metal doping of graphene supported on non-noble metal substrates researchers are able to achieve an optimum solution for a versatile and cheaper electrode with excellent activity towards catalysis.

In this work, by means of dispersion-corrected density functional theory (DFT) calculations, we investigate structural, electronic and energetic properties of four non-noble SACs, namely Fe, Co, Ni and Cu, trapped at the single (1VG) and double (2VG) carbon vacancies in graphene. This is followed by the N-doping of these structures through substitution of the C atoms at the edges of the defects. In the 2VG hole, the TM atoms acquire a pseudo-square planar coordination, similar to what observed in macrocyclic ligands, such as porphyrins. Given this analogy, the electronic properties of the SAC centers are discussed in terms of the TM d-orbitals splitting according to the crystal/ligand field theories. The resulting molecular orbital (MO) diagrams, when used in combination with the projected density of states (PDOS), help in understanding not only the bonding between the TM and graphene but also serves as a fundamental reference for the Cu(111) and Ni(111) supported systems, since the variations in the TM d-orbital peak position around the Fermi occur due to the interaction with the substrate. The choice of these two underlying substrates is not only because of their common use in experiments,[12,18] but also because of the weak (with Cu) and strong (with Ni) interactions of the graphene layer, which allows exploring the two extreme scenarios. Finally, we also compute the differential Gibb's free energy (ΔG_{H*}) for hydrogen adsorption at the SACs to shed light onto its catalytic activity towards HER under various conditions.

2. Methods

We used density functional theory (DFT) simulations with plane wave basis in this study as implemented in the Quantum Espresso suite.[27] Ultrasoft pseudo potentials requiring wave-function

and charge density cut-offs of 46 Ry and 401 Ry were used. A 6×6-unit cell was used to model the free-standing as well as the supported graphene. The Cu(111) and Ni(111) slabs were modelled by using the lattice constant of 2.46 Å, of graphene. Each of these slabs were constructed with three atomic layers where the bottom-most layer was kept fixed during all relaxations. A vacuum of more than 20 Å was introduced between the slabs to avoid the spurious interactions between the periodic cells in the z-direction. The energy convergence threshold was set to 10^{-6} Ry and forces were converged until they were as low as 10^{-3} Ry. $Bohr^{-1}$. A 3×3×1 Monkhorst-Pack[28] k-points grid was used to sample the Brillouin zone. For PDOS we did the convergence test until a 12×12×1 k-mesh and since the PDOS features remain unchanged, only the ones obtained for 3×3×1 are shown here. To consider the van der Waal's interactions all calculations were performed including the vdw-DF2-c09 non-local functional.[29-32] The ball and stick models were produced by using the XCrySDen software[33].

In order to simulate HER, we followed Nørskov's methodology to model the electrochemical half-cell[34]. Applying the computational hydrogen electrode (CHE) approach, the chemical potential of the electron-hole ($H^+ + e^-$) pair can be replaced by that of half the hydrogen molecule. When no external potential is applied, at pH=0, T=298.15 K and 1 bar of H_2, the reaction: $H^+ + e^- \leftrightarrow ½\ H_2$ is in equilibrium; i.e., the free energy per H atom of the initial state is equal to that of the final state. Employing this method, first the electronic energy of atomic hydrogen adsorption (ΔE_{H^*}) is calculated as: $\Delta E_{H^*} = E_{sys+nH} - E_{sys+(n-1)H} - ½\ E_{H_2}$), where E_{sys+H} is the total energy of the system with "n" H atoms adsorbed, $E_{sys+(n-1)H}$ is the energy of the system with "n-1" H atoms adsorbed and E_{H_2} is the energy of an H_2 molecule. Once we have the electronic energy, the Gibb's free energy for atomic hydrogen adsorption ΔG_{H^*}, which is the key descriptor of HER activity used in simulations, can be obtained as follows: $\Delta G_{H^*} = \Delta E_{H^*} + \Delta ZPE_{H^*} - T\Delta S_{H^*}$. ΔZPE_{H^*} is the zero point energy difference obtained as $\Delta ZPE_{H^*} = ZPE_{nH} - ZPE_{(n-1)H} - ½\ ZPE_{H_2}$ where ZPE_{nH} is the zero point energy of the "n" adsorbed H atoms present in the system and ZPE_{H_2} is the zero point energy of the H_2 molecule. The ZPEs are obtained by computing the vibrational frequencies (converted to eV) of the adsorbed H atoms in the former and that of the molecular hydrogen in the latter, computed within the density functional perturbation theory (DFPT) using the PH code of Quantum Espresso[27]. Similarly, ΔS_{H^*} is the difference in entropies between the adsorbed H atoms and the H_2 molecule. The entropy of the H_2 molecule is taken as TS_{H_2}=0.41 eV, under standard

conditions[35]. According to Sabatier principle, in the ideal case, the best catalyst has a value of $\Delta G_{H^*} \approx 0$ eV which indicates thermoneutrality.

3. Results and discussion

3.1 Undoped Graphene on Metals

Pristine graphene adsorbed on Cu(111) and Ni(111) has been investigated before in the literature[11]. Here, we report the results obtained with our computational setup to prove the agreement with previous works,[11,36] as discussed below, but also for comparison with the modified systems in the next sections. The optimized geometries obtained for these two systems are shown in Figures S3(a) and (e) of the Supplementary Material. Graphene interacts very differently with these two metals.[11] The interaction is rather weak with Cu, resulting in an adsorption energy of -3.66 eV, whereas, on the contrary, it is extremely strong with Ni, with an adsorption energy of -7.68 eV. In fact, the electronic states of graphene remain quite intact on the former while on the latter the characteristic Dirac point of graphene is strongly modified[36] as shown in Figure S1 of the Supplementary Material. This difference in interaction is also very much evident in the geometry, as the adsorption distances between the graphene layer and Ni(111) surface or Cu(111) surface are of 2.10 Å and 3.24 Å, respectively. These values are in accordance with those measured, as well as with those previously calculated in the literature.[11,36,37] On both of these substrates, graphene is slightly n-doped (see Figure S1).[36]

We remark that, as references for our analysis in the next sections, we have also simulated both the empty carbon single vacancy (1VG) and double vacancy (2VG), with and without substitutional N doping on free-standing as well as supported graphene, as reported in the Supplementary Information (see Figures S2, S3, and S4).

3.2 TM (Fe, Co Ni Cu) atoms trapped in free-standing graphene

In this section we present the SAC systems, i.e. the metal atoms trapped at the 1VG and 2VG of graphene. We have chosen four non-noble transition metal (TM) atoms, namely Fe, Co, Ni and Cu, which would have great potentials as cheap catalysts. Cu and Ni may even result as trapped intrinsic adatoms emerging from the substrate itself.

Analyzing these TMs, Fe and Ni have an even number of electrons while Cu and Co have an odd number. Cu is the only diamagnetic (bulk) material in nature while all the others are ferromagnetic.

Also, Cu is the only one with a completely filled d-orbital among the four. Just with these properties in mind we can predict beforehand an unalike behavior from Cu compared to the other three.

First, we have considered one TM atom encapsulated at a single C vacancy (1VG) in free-standing graphene. The optimized geometries obtained for the four TMs are shown in Figure 1(a-d). From the side views it is evident that none of the metal adatoms are lying in the same plane as graphene. The TMs in Fe@1VG, Co@1VG, Ni@1VG and Cu@1VG are at heights of 1.37 Å, 1.33 Å, 1.34 Å, 1.46 Å with respect to the averaged height of the C atoms in the graphene layer, respectively. We also computed the energy cost to go through the 1VG, by means of a constrained geometry optimization of the TM fixed in the plane of the C layer. Depending on the TM the energy cost goes from 2.1 (Cu) up to 2.8 (Fe) eV. The results are shown in Figure S5 of the Supplementary Information. All the observations above clearly point to the fact that the 1VG defect is too small to accommodate (in-plane) any of the TM atoms considered.[38]

Therefore, we moved to consider a larger sized defect, the double C vacancy (2VG), where the TM atoms are found to lie in the same plane as graphene, as evident from the side views of the relaxed geometries of the free-standing TM@2VG systems in Figure 2(a-d). More details of the structural parameters, such as the values of α, α'; θ, θ' and TM-C bond lengths are given in Table 1. One can easily recognize that the structures of the TM@2VG are reminiscent of a square-planar geometry, a well-known type of coordination in TM complexes. However, in an ideal square planar structure all the angles marked in Figure 2(a) should be equal to 90° and all the bonds forming these angles should be of equal length. Our TM@2VG systems show minor variations from these features, except for Co@2VG exhibiting the largest deviation of +24.2° for α and of -9.3° for θ, followed by Fe@2VG. Ni@2VG and Cu@2VG instead are very close to ideal and manifest the same angle values, with a slight difference in TM-C bond length (1.87 vs 1.89 Å).

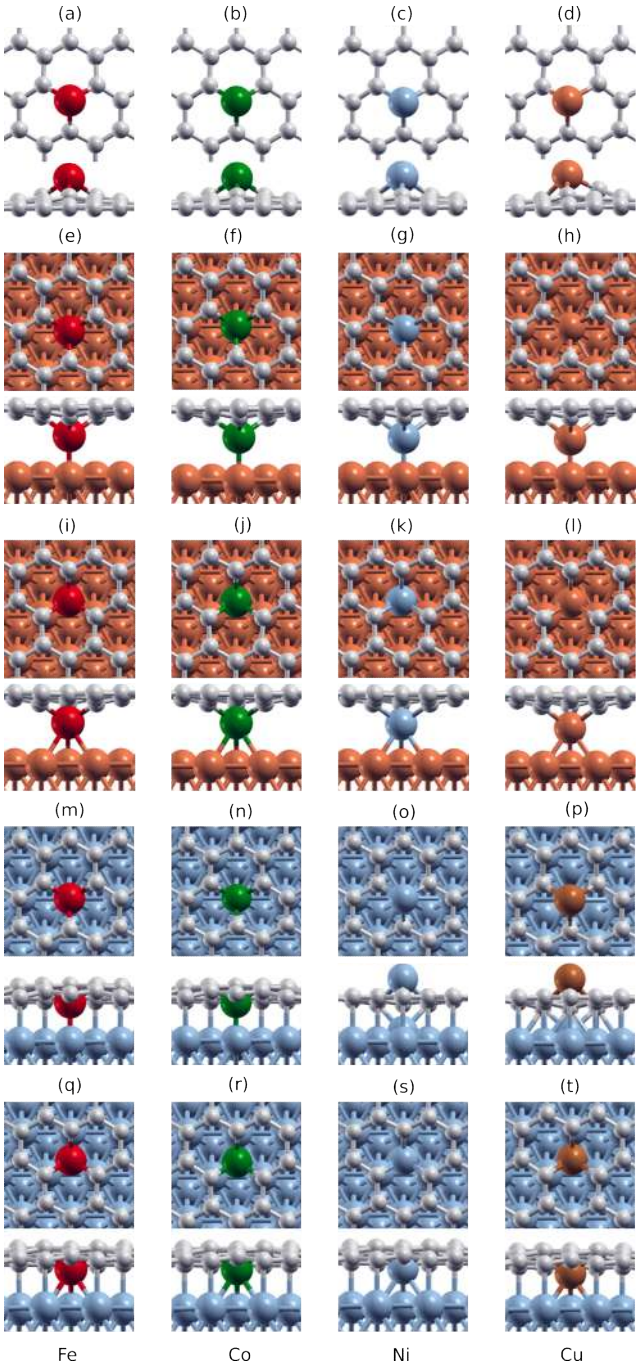

Figure 1: Optimized structures of free-standing (a) Fe@1VG, (b) Co@1VG, (c) Ni@1VG, (d) Cu@1VG, and supported at the top site of Cu(111) (e) Fe@1VG/Cu(111), (f) Co@1VG/Cu(111), (g) Ni@1VG/Cu(111), (h) Cu@1VG/Cu(111), at the fcc site of Cu (111) (i) Fe@1VG/Cu(111), (j) Co@1VG/Cu(111), (k) Ni@1VG/Cu(111), (l) Cu@1VG/Cu(111), at the top site of Ni(111) (m) Fe@1VG/Ni(111), (n) Co@1VG/Ni(111), (o) Ni@1VG/Ni(111), and (p) Cu@1VG/Ni(111), at the fcc site of Ni(111) (q) Fe@1VG/Ni(111), (r) Co@1VG/Ni(111), (s) Ni@1VG/Ni(111), and (t) Cu@1VG/Ni(111).

Table 1: The structural parameters of the optimized geometries shown in Figure 2 are reported here. The angles α, α' and θ, θ' are as marked in Figure 2. TM-C is the average bond length between the metal adatom and the four C atoms to which it is bonded (the standard deviation is given in brackets). In the case of the supported systems the buckling of the graphene layer, the height of the metal adatom and the height of the farthest C atom both with respect to the average height of the first layer atoms of the substrate are also given.

Free-standing	Fe@2VG	Co@2VG	Ni@2VG	Cu@2VG
α, α'	87.8°, 99.5°	114.2°, 84.5°	92.2°, 92.2°	92.1°, 92.1°
θ, θ'	86.4°, 86.4°	80.7°, 80.7°	87.8°, 87.8°	87.9°, 87.9°
TM-C Bond Length (Å)	1.99 (±0.04)	1.88 (±0.10)	1.87 (±0.00)	1.89 (±0.00)
Magnetism on TM (μB)	2.97	0.58	0.00	0.01
Supported on Cu(111)				
α, α'	88.8°, 87.8°	89.2°, 89.2°	90.4°, 90.4°	91.4°, 91.4°
θ, θ'	84.8°, 84.7°	86.5°, 86.2°	87.7°, 87.5°	88.0°, 87.9°
TM-C Bond Length (Å)	1.92 (±0.04)	1.93 (±0.10)	1.92 (±0.00)	1.92 (±0.00)
Buckling of G (Å)	0.99	1.02	1.03	0.97
TM height (Å)	1.89	1.94	2.08	2.24
Highest C (Å)	3.06	3.06	3.06	3.07
Magnetism on TM (μB)	1.06	-0.00	0.00	-0.00
Supported on Ni(111)				
α, α'	89.8°, 89.8°	91.5°, 91.5°	92.4°, 92.4°	92.4°, 92.4°
θ, θ'	84.6°, 84.8°	87.0°, 86.2°	88.0°, 87.3°	88.0°, 86.2°
TM-C Bond Length (Å)	1.88 (±0.00)	1.87 (±0.00)	1.85 (±0.01)	1.87 (±0.01)
Buckling of G (Å)	0.15	0.19	0.15	0.16
TM height (Å)	1.65	1.79	2.06	2.19
Highest C (Å)	2.20	2.18	2.14	2.14
Magnetism on TM (μB)	0.03	0.48	0.07	-0.01

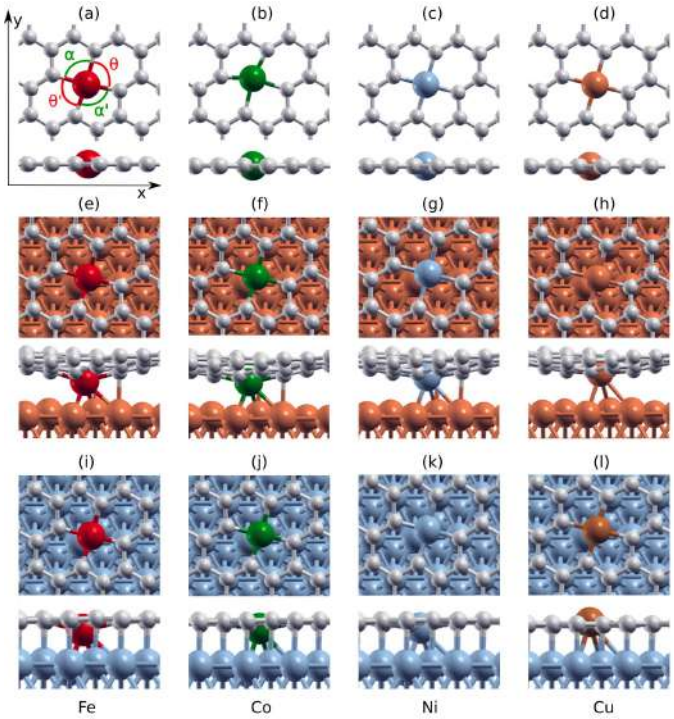

Figure 2: Optimized structures of free-standing (a) Fe@2VG, (b) Co@2VG, (c) Ni@2VG, (d) Cu@2VG, those supported on Cu(111) (e) Fe@2VG/Cu(111), (f) Co@2VG/Cu(111), (g) Ni@2VG/Cu(111), (h) Cu@2VG/Cu(111), and those supported on Ni(111) (i) Fe@2VG/Ni(111), (j) Co@2VG/Ni(111), (k) Ni@2VG/Ni(111), and (l) Cu@2VG/Ni(111).

According to the crystal field theory, the d-orbitals of a transition metal atom at the center of a square-planar structure with D_{4h} symmetry are split in the following order: the most stable are the degenerate d_{xz} and d_{yz}, followed by d_{z^2}, d_{xy}, and $d_{x^2-y^2}$ respectively. Following the ligand field theory, the split d-orbitals, when approached by the orbitals of the ligands with proper symmetry, give rise to σ and π bonding and anti-bonding molecular orbitals. In the present case, where the ligands are C atoms in the defective graphene network, the ligand orbitals are sp^2 and p_z orbitals of the unsaturated C atoms at the 2VG center. Hence, the d-orbitals of the TM atom mix up with the in-plane sp^2 hybridized orbitals and the p_z of the four C atoms in the square planar structure, producing a new set of molecular orbitals, as sketched in the schemes of Figure 3, where the order and the nature of these resulting molecular orbitals for each of the TM@2VG systems are presented. The schemes are derived from the electronic structure calculations in terms of projected densities of states (PDOS) of these free-standing systems, which will be discussed below and are reported in the first column of Figure 4. In all the PDOS graph we have highlighted the (d_{xy} - σ*) energy separation because we consider it a reliable descriptor of the extent of ligand field splitting because, whereas the σ states are rather widely spread in energy,

the occupied non-bonding d_{xy} state is highly localized and should not be affected by the presence of the underlying substrate. This descriptor will be often used in the discussion in this and in the next sections.

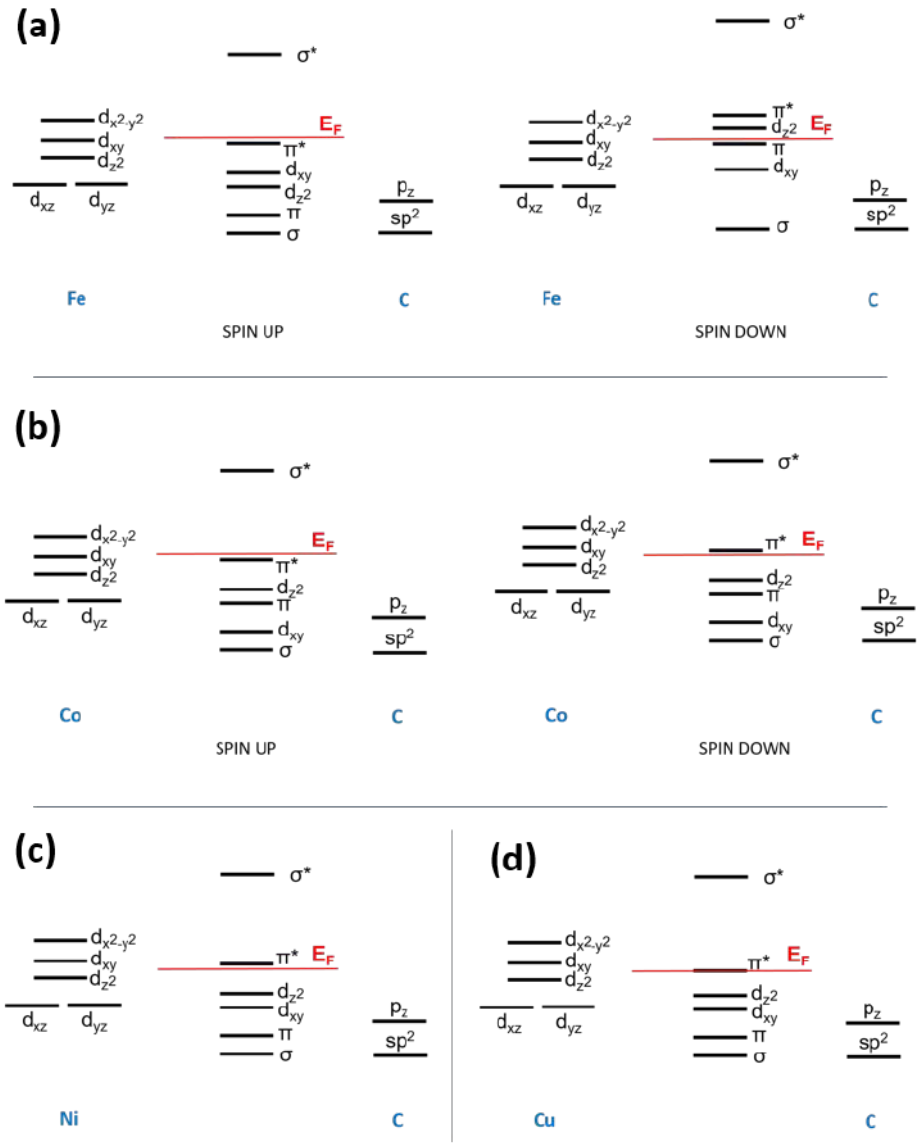

Figure 3: MO diagrams of free standing (a) Fe@2VG (b) Co@2VG (c) Ni@2VG (d) Cu@2VG. Relative position of the levels is derived from the PDOS in Figure 4.

For the two magnetic systems, Fe@2VG and Co@2VG, both the spin-up and spin-down components are shown separately in Figure 3 (a and b). We start by examining thoroughly the spin-up component of the Fe@2VG MO diagram in Figure 3(a). We can observe that the $d_{x^2-y^2}$ orbital of Fe overlaps with the four sp^2 orbitals of neighboring C atoms. This in-plane interaction results in bonding and anti-binding σ orbitals. Next the degenerate d_{xz}, d_{yz} orbitals of Fe overlap with the p_z of the

neighboring C atoms, giving rise to bonding and anti-bonding π orbitals, as marked in the scheme. The d_{xy} and d_{z^2} orbitals remain non-bonding, the latter however gets more stabilized than the former. Therefore, the resulting orbitals ordering is: σ, π, d_{z^2}, d_{xy}, π* and σ*. The same scheme of orbital mixing occurs for the spin-down components with the only difference in the ordering of the resulting orbitals: σ, d_{xy}, π, d_{z^2}, π*, and σ*. Hence, the d_{xy} orbital appears to be stabilized.

The case of Co@2VG, even though quite similar to Fe@2VG, still presents some peculiarities. In the MO diagram of Figure 3(b), we observe that the d_{xy} orbital of Co is found to split into bonding and anti-bonding orbitals in both the spin-up and spin-down components. This could be attributed to the heavy in-plane geometrical distortion from a perfect square planar structure as discussed above (see Figure 2(b)). The very α angle causes the involvement of both the $d_{x^2-y^2}$ and d_{xy} in coordination with the four coordinating C atoms. The d_{z^2} orbital is below the Fermi energy level, hence, it is occupied, both in the spin-up and in the spin-down. Thus, the orbital ordering for both the spins is: σ($d_{x^2-y^2}$), σ(d_{xy}), π, d_{z^2}, π*, σ*(d_{xy}), and σ*($d_{x^2-y^2}$).

For the non-magnetic Ni@2VG and Cu@2VG systems the MO schemes are shown in Figure 3(c) and (d), where the resulting orbital ordering is found to be as follows: σ, π, d_{xy}, d_{z^2}, π*, and σ*. The only difference between them being that the π*, which is above the Fermi energy (unoccupied) in Ni@2VG, is almost below the Fermi (occupied) in Cu@2VG.

As mentioned above, the MO schemes have been derived from the projected density of states (PDOS) of these systems, which are shown in Figure 4(a-d). PDOS provide more quantitative information than the MO schemes. Since the d-orbitals are the valence orbitals of the TM atom, it is fundamental to determine their energy level alignment with respect to the Fermi level of the whole system for their use in technological devices. If we notice carefully, the spin-up component of the π* of Fe@2VG is pinned to the Fermi level, whereas that of Co@2VG is filled. In the case of Ni@2VG it remains unoccupied while for Cu it gets almost filled. This trend confirms that the Cu d states are the deepest in energy among the TMs considered, since it presents the largest atomic number with the most attractive nucleus for the 3d states. We explicitly marked the energy difference between the occupied d_{xy} and the unoccupied σ($d_{x^2-y^2}$) because we consider this a reliable parameter to estimate the extent of the crystal/ligand field splitting and also we expect those two states to be the least involved in the interaction with the underlying substrate, which will be investigated in Section 3.4. The largest separation of these orbitals is observed for Fe@2VG with a value of 6.01 eV, followed by 5.91 eV for Cu@2VG, 5.50 eV for Co@2VG and finally 5.35 eV for Ni@2VG.

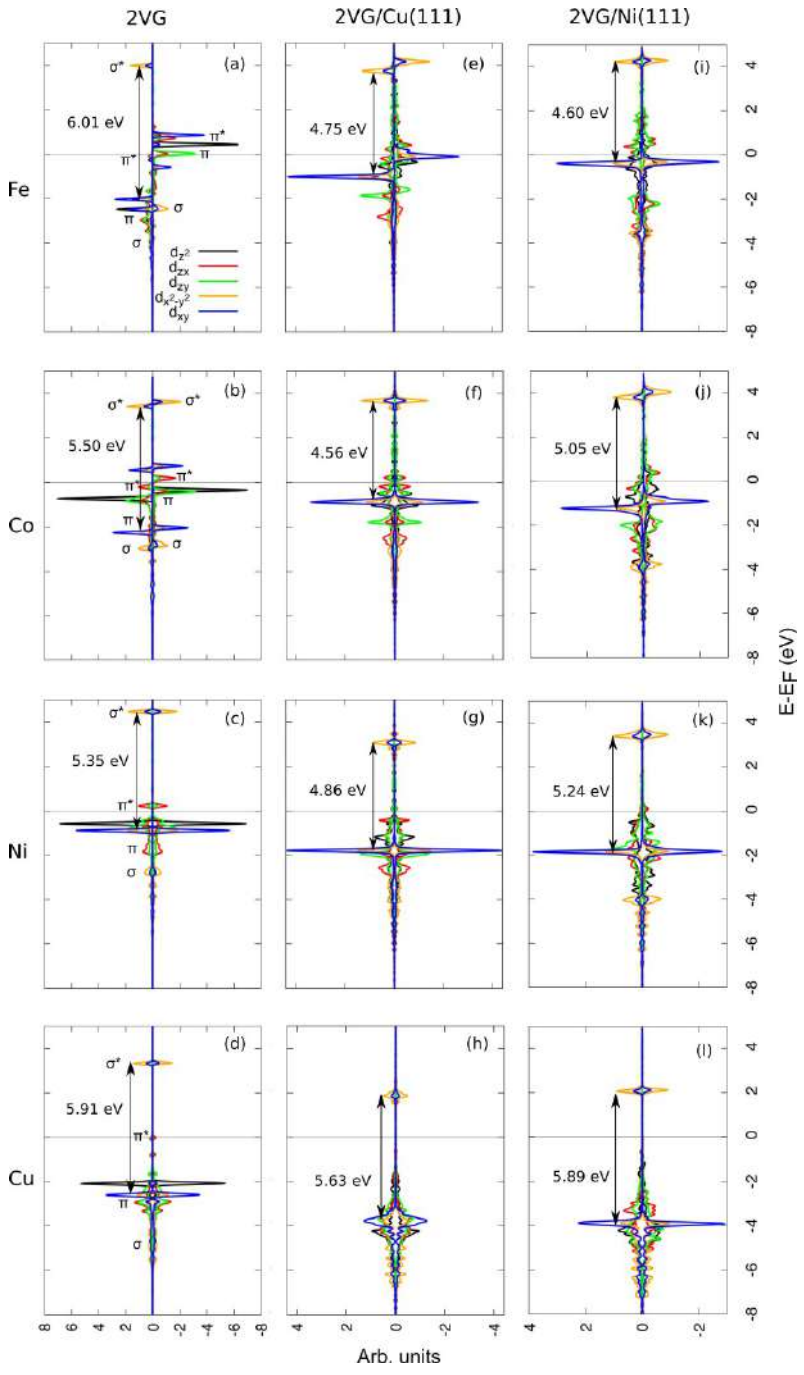

Figure 4: PDOS on the d-states of the transition metal adatom in free-standing (a) Fe@2VG, (b) Co@2VG, (c) Ni@2VG, (d) Cu@2VG, and supported (e) Fe@2VG/Cu(111), (f) Co@2VG/Cu(111), (g) Ni@2VG/Cu(111), (h) Cu@2VG/Cu(111), (i) Fe@2VG/Ni(111), (j) Co@2VG/Ni(111), (k) Ni@2VG/Ni(111), and (l) Cu@2VG/Ni(111).

3.3 TM (Fe, Co Ni Cu) trapped in N-doped free-standing G

It is known that the interposition of nitrogen atoms enhances the stability of the bond between the TM atom and the graphene network,[19] similarly to what is observed in metal porphyrins. Therefore, we have replaced the C atoms bonded to the TM atom with N atoms.

First, we investigated the N-doped 1VG in free-standing graphene (TM@3N1VG), as shown in Figure 5(a-d). The side views of these structures show that all the TM atoms lie in the same plane of the graphene layer, which was not the case in the absence of the N atoms (see Figure 1(a-d)).

Then, we replaced the four C atoms in the 2VG model with four N atoms (TM@4N2VG), as shown in Figure 6(a-d), where all the TM atoms considered lie in the plane of the graphene layer. Additional structural parameters of TM@4N2VG are reported in Table 2. The values of the angles α, α' are the same, the θ, θ' are the same, as well as all the TM-N bond lengths. These results indicate a more symmetrical square-planar structure of TM@4N2VG in comparison with those of TM@2VG. In particular, the most distorted among the TM@2VG systems, Co@2VG, with α of 114° and α' of 84°, is now modified to α = α' = 92° in the presence of N in Co@4N2VG. In short, one can say that the substitution with N atoms has improved the structural symmetry and hence stability of the TM atoms in graphene.

In the following, we will discuss the effect of the N-doping on the electronic properties of the free-standing TM@4N2VG with respect to free-standing TM@2VG. The MO diagrams and the PDOS of these systems are shown in Figure 7 and 8, respectively. The MO schemes are derived from their corresponding PDOS as already discussed in the previous section. We first look at the MO diagram of Fe@2V4NG in Figure 7(a). This is the only spin-polarized system among all the free-standing nitrogen-doped cases. The d-orbitals of the TM atom overlap with the hybridized sp^2 and with the p_z states of the N atoms (similarly to the C atoms in the previous section) to form σ and π bonding and anti-bonding molecular orbitals. In-plane interactions between the $d_{x^2-y^2}$ orbital of Fe with the four sp^2 orbitals of the neighboring N atoms results in bonding and anti-bonding σ orbitals. While the out-of-plane d_{xz}, d_{yz} orbitals of Fe interact with the p_z of the neighboring N atoms, giving rise to bonding and anti-bonding π orbitals. As for Fe@2VG (without N doping), the d_{xy} and d_{z^2} orbitals remain non-bonding. Hence, the orbital order here for the spin-up is σ, π, d_{z^2}, π*, d_{xy} and σ* with the Fermi energy above the d_{xy} with an inversion between d_{xy} and π* with respect to what was observed for Fe@2VG, whereas for the spin-down component it is σ, π, d_{xy}, d_{z^2}, π*, and σ* with the Fermi energy just above the d_{xy}, with only an inversion between d_{xy} and π with respect to what was observed for Fe@2VG.

Figure 7 shows the MO schemes of (b) Co@4N2VG, (c) Ni@4N2VG, and (d) Cu@4N2VG where the orbital ordering for all of them are σ, d_{xy}, π, d_{z^2}, π*, and σ*. We now examine the PDOS of Figures 8(a-d) from which these MO schemes were derived from. A general comment about the PDOS is that all the peaks are sharper with slightly higher amplitudes than their non-N-doped counterparts TM@2VG (see Figures 4(a-d)). This is due to the improved geometrical symmetry brought forth by the N atoms in the structure, as discussed before.

The PDOS of Fe@4N2VG is shown in Figure 8(a), where the Fe d_{x2-y2} state is found to interact not just with the sp^2 states of N but with several band states of the graphene lattice. Hence, the resulting bonding σ states are rather dispersed in energy or in other words, the corresponding peak is extremely spread over a large energy range (from -7 to -4 eV). The Fe d_{xz} and d_{yz} interact with the N p_z to form π and π* MO. The d_{z^2} and d_{xy} remain non-bonding but the d_{xy} gets slightly destabilized with respect to the situation in Fe@2VG. Regarding magnetism, in Fe@4N2VG it is almost 1 μB smaller than it was in Fe@2VG (see Tables 1 and 2), which is also visible in their respective PDOS. The (d_{xy} - σ*) separation for the spin-up component of Fe@4N2VG is only 3.68 eV compared to that of Fe@2VG that was 6.01 eV. This huge reduction is partly because the d_{xy} has moved to higher energy and mostly because the σ* has been displaced to much lower energy values. The motivation for this behavior is that the ligand orbitals taking part in the hybridization with the d-orbitals of the TM are the sp^2 and p_z of the N atoms, unlike those of the C atoms in Fe@2VG. Since, the N states are deeper in energy than the C states, the σ and σ* orbitals in Fe@4N2VG are rigidly shifted to lower energies than in Fe@2VG. A reduction of the (d_{xy} - σ*) separation is observed for all the TM@4N2VG cases with respect to the corresponding TM@2VG by more than 2 eV.

Similarly, to what is observed for Fe@4N2VG, also in the case of Co@4N2VG the σ(d_{x2-y2}) is quite dispersed. The Fermi energy is at the π*. With respect to Co@2VG, which had a clear σ peak at around -3 eV (see Figure 4(b)), in Co@4N2VG (Figure 8(b)) the σ peak is of very low amplitude and broadly spread due to heavy dispersion, as mentioned before. Again here, the (d_{xy} - σ*) separation in Co@4N2VG is 2 eV smaller than that in Co@2VG for the same reasons discussed above. Additionally, the magnetization of 0.58 μB, which was present in Co@2VG is instead completely quenched in Co@4N2VG, which is non-magnetic, as also evident from the PDOS.

In the case of Ni@4N2VG, the σ peak, which was otherwise more pronounced in Ni@2VG, is shallow and broadly extends over a large energy range (compare Figures 8(c) and 4(c), respectively). The d_{xy} gets stabilized and π* gets filled. Due to the same reason the (d_{xy} - σ*) separation reduces by 1.77 eV for Ni@4N2VG compared to its non-N-doped counterpart.

The scheme of Cu@4N2VG is very similar to that of Ni@4N2VG except that the σ* orbital is at the Fermi level since Cu d states are the deepest when compared to Ni, Co and Fe. Here, the (d_{xy} - σ*) separation reduces by 2.31 eV for Cu@4N2VG compared to its non-N-doped counterpart, Cu@2VG (see Figures 8(d) and 4(d)).

From this comparative analysis of the PDOS, we conclude that the Cu d states are the deepest with respect to the Fermi level than any of the other TMs considered in this work. From the approximate estimation of the Löwdin charges on the TM atoms (reported in Table S1 of the Supplementary Information) we may also note that Cu atom, when trapped in defective free-standing (also N-doped) graphene, always presents a positive charge, which most of the times is the highest among the four TMs considered.

3.4 Metal-supported systems

3.4.1 Fe, Co, Ni, Cu @ G on Cu(111) and Ni(111)

The study now proceeds with the deposition of the free-standing TM@1VG and TM@2VG structures over a weakly interacting and a strongly interacting metal substrates, namely Cu(111) and Ni(111).[36] The presence of the substrate may affect both the structural and electronic properties of the TM-doped graphene layer. In the most stable configurations, the registry of the C atoms of graphene with the metal substrate is such that they occupy the top and fcc sites.

For the TM@1VG systems, we consider the TM atom at both top and fcc sites as per the graphene registry with the metal substrates since the TM atom is a replacement of a graphene C atom. In the case of Fe@1VG/Cu(111), the top site is favored with respect to the fcc site by -0.35 eV. In the case of Co@1VG/Cu(111), Ni@1VG/Cu(111) and Cu@1VG/Cu(111), the fcc is more stable than the top site by -0.23, -0.32 and -0.45 eV, respectively. The optimized configurations of TM@1VG/Cu(111) at top and fcc sites are shown in Figures 1(e-h) and (i-l) respectively. From the side views, it is evident that, when the TM atom is at the top site, it forms direct bond with the Cu atom below with bond lengths obtained for Fe-Cu, Co-Cu, Ni-Cu, and Cu-Cu are 2.26 Å, 2.24 Å, 2.21 Å, and 2.18 Å, respectively. Differently, at the fcc site one can observe that the TM atom forms three bonds with the three Cu atoms underneath. The bond lengths calculated with respect to the averaged heights of the first layer Cu atoms for Fe-Cu, Co-Cu, Ni-Cu, and Cu-Cu are 1.95 Å, 1.98 Å, 1.89 Å, and 1.80 Å, respectively. In all these cases, however, the TM atom lies between the plane of graphene and the Cu substrate (downward configuration).

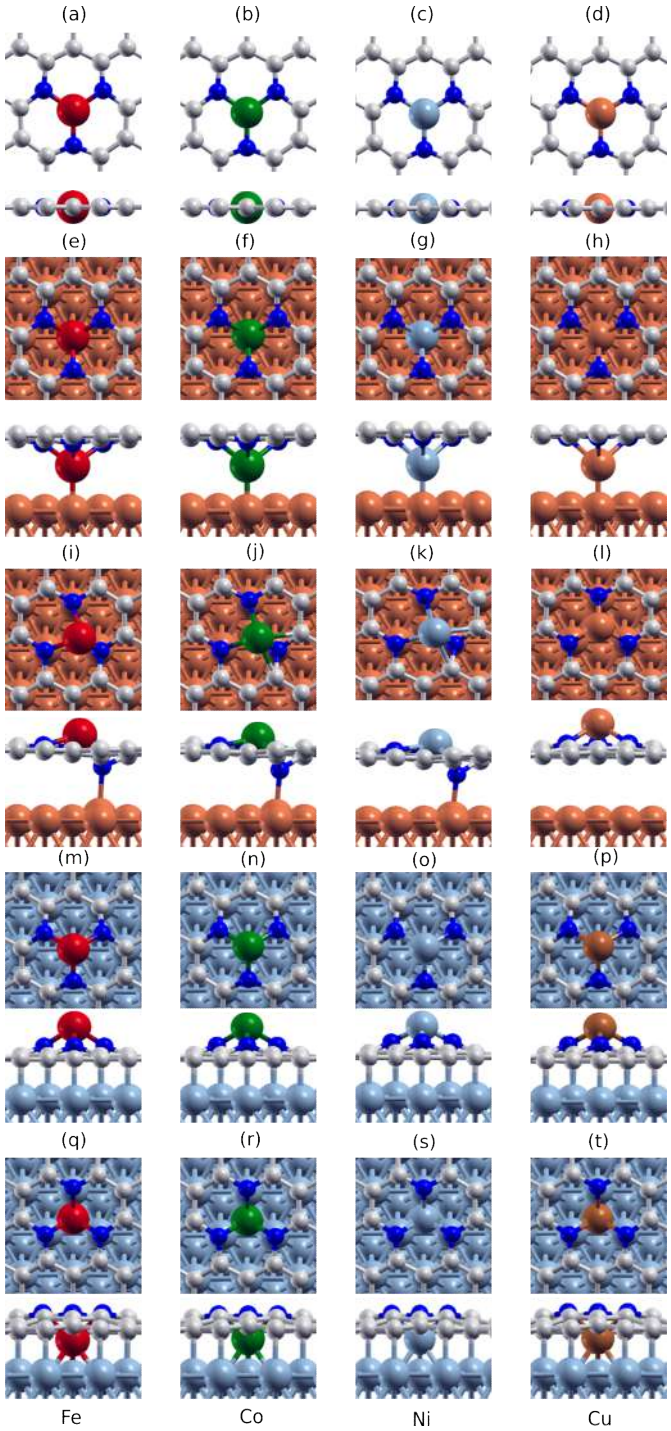

Figure 5: Optimized structures of nitrogen-doped free-standing (a) Fe@3N1VG, (b) Co@3N1VG, (c) Ni@3N1VG, (d) Cu@3N1VG, and supported at the top site (e) Fe@3N1VG/Cu(111), (f) Co@3N1VG/Cu(111), (g) Ni@3N1VG/Cu(111), (h) Cu@3N1VG/Cu(111), at the fcc site (i) Fe@3N1VG/Cu(111), (j) Co@3N1VG/Cu(111), (k) Ni@3N1VG/Cu(111), (l) Cu@3N1VG/Cu(111), at the top site (m) Fe@3N1VG/Ni(111), (n) Co@3N1VG/Ni(111), (o) Ni@3N1VG/Ni(111), and (p) Cu@3N1VG/Ni(111), at the fcc site (q) Fe@3N1VG/Ni(111), (r) Co@3N1VG/Ni(111), (s) Ni@3N1VG/Ni(111), and (t) Cu@3N1VG/Ni(111).

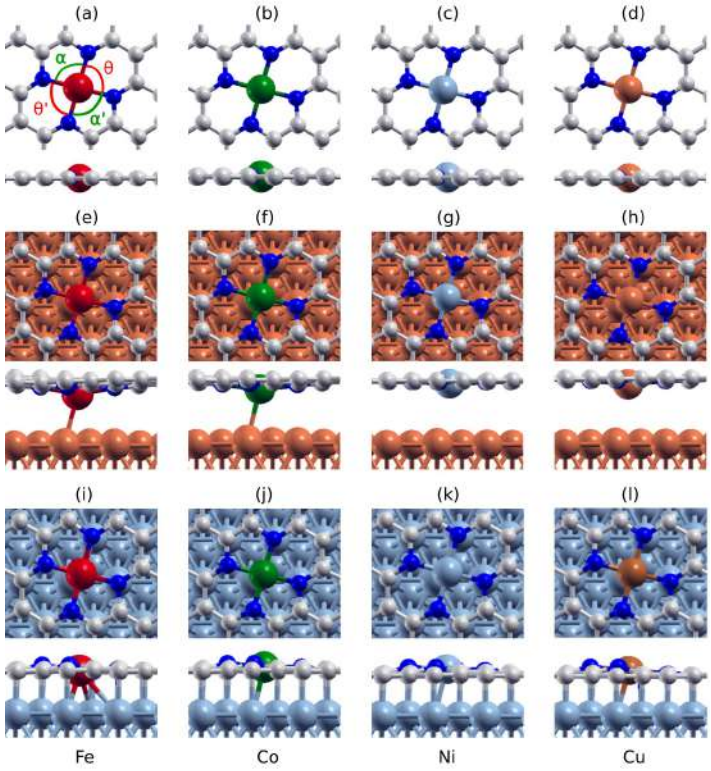

Figure 6: Optimized structures of free-standing (a) Fe@4N2VG, (b) Co@4N2VG, (c) Ni@4N2VG, (d) Cu@4N2VG, and supported (e) Fe@4N2VG/Cu(111), (f) Co@4N2VG/Cu(111), (g) Ni@4N2VG/Cu(111), (h) Cu@4N2VG/Cu(111), (i) Fe@4N2VG/Ni(111), (j) Co@4N2VG/Ni(111), (k) Ni@4N2VG/Ni(111), and (l) Cu@4N2VG/Ni(111).

The scenario is slightly different in the case of the Ni(111) substrate due to its much stronger interaction with G. The separation between G and Ni(111) is almost 1 Å smaller than that between G and Cu(111). The optimized geometries of TM@1VG/Ni(111) at top and fcc sites are shown in Figures 1(m-p) and (q-t), respectively. The Fe and Co atoms at the top sites lie almost in the graphene plane while Ni and Cu are out of the plane of the graphene layer (upward configuration). All the TMs are slightly more out-of-plane when on the fcc sites. While in the case of top sites, the bond lengths for Fe-Ni, Co-Ni, Ni-Ni, and Cu-Ni are 2.18 Å, 2.15 Å, 2.49 Å, and 2.55 Å, in the case of fcc sites the values are 1.85 Å, 1.86 Å, 1.81 Å, and 1.78 Å, respectively. The latter is computed with respect to the averaged heights of the first layer atoms of the Ni surface.

Table 2: The structural parameters of the optimized geometries shown in Figure 6 are reported here. The angles α, α' and θ, θ' are as marked in Figure 6. TM-N is the average bond length between the metal adatom and the four N atoms to which it is bonded (the standard deviation is given in brackets). In the case of the supported systems the buckling of the graphene layer considering only the C atoms

(G) and both the N and C atoms (NG), the height of the metal adatom and the height of the farthest C atom both with respect to the averaged height of the first layer atoms of the substrate are also given.

Free-standing	Fe@4N2VG	Co@4N2VG	Ni@4N2VG	Cu@4N2VG
α, α’	91.4°, 91.4°	91.6°, 91.6°	91.6°, 91.6°	91.7°, 91.7°
θ, θ’	88.6°, 88.6°	88.4°, 88.4°	88.4°, 88.4°	88.3°, 88.3°
TM-N Bond Length (Å)	1.89 (±0.00)	1.87 (±0.00)	1.87 (±0.00)	1.92 (±0.00)
Magnetism on TM (μB)	2.06	-0.01	-0.00	0.00
Supported on Cu(111)				
α, α’	89.3°, 89.3°	90.9°, 90.9°	91.5°,9 1.5°	91.2°, 91.2°
θ, θ’	87.3°, 87.0°	87.9°, 87.9°	88.2°, 88.4°	87.8°, 87.8°
TM-N Bond Length (Å)	1.91 (±0.00)	1.88 (±0.01)	1.87 (±0.00)	1.93 (±0.00)
Buckling of G (Å)	0.40	0.28	0.08	0.10
Buckling of NG (Å)	0.52	0.37	0.10	0.13
TM height (Å)	2.54	2.74	3.10	2.98
Highest C (Å)	3.17	3.22	3.25	3.26
Magnetism on TM (μB)	1.29	-0.00	-0.00	0.48
Supported on Ni(111)				
α, α’	91.1°, 91.1°	91.6°, 91.6°	91.8°, 91.8°	92.1°, 92.1°
θ, θ’	87.3°, 88.5°	87.9°, 88.7°	88.6°, 87.8°	86.0°, 90.0°
TM-N Bond Length (Å)	1.88 (±0.02)	1.86 (±0.01)	1.87 (±0.01)	1.92 (±0.02)
Buckling of G (Å)	0.16	0.15	0.21	0.18
Buckling of NG (Å)	0.33	0.37	0.46	0.51
TM height (Å)	2.14	2.29	2.40	2.36
Highest C (Å)	2.23	2.22	2.26	2.24
Magnetism on TM (μB)	1.38	0.04	-0.01	0.38

Energy-wise, for Fe@1VG/Ni(111) and Co@1VG/Ni(111), the fcc site is favoured than the top by -0.29 eV and -0.43 eV, while for Ni@1VG/Ni(111) and Cu@1VG/Ni(111) the top site is favoured by -0.66 eV and -1.47 eV, respectively. From these results, we may conclude that the more stable structures in the case of Ni@1VG/Ni(111) and Cu@1VG/Ni(111) are those where the TM atom is protruding away from the surface (see Figures 1 (o and p)). We have estimated the energy barrier to pass through the 1VG, going from an upward to a downward configuration, when the smallest TM atom (Cu) is on an fcc site on the Ni(111) surface, see Figure S6 of the Supplementary Information. This is a lower bound limit for the other TM atoms and it is 1.83 eV. Considering that the corresponding barrier for Cu to go through 1VG in free-standing graphene was 2.07 eV (in Figure S5), we may conclude that the presence of the Ni(111) substrate slightly favours this process.

The relaxed structures of the TM adatoms trapped at the double vacancy on Cu(111) are shown in Figure 2(e-h). The square-planar structures look quite symmetric from the top view. This is indeed confirmed quantitatively by the values of the bond angles and bond-lengths in Table 1. The square-planar symmetry is higher here than for the free-standing structures. From the side views, it looks like the TMs are pulled down by the Cu substrate, thereby pulling along with them also the attached C atoms of graphene. Hence, the graphene layer is buckled by around 1 Å in all the cases. Fe is the closest adatom to the substrate followed by Co, Ni and Cu.

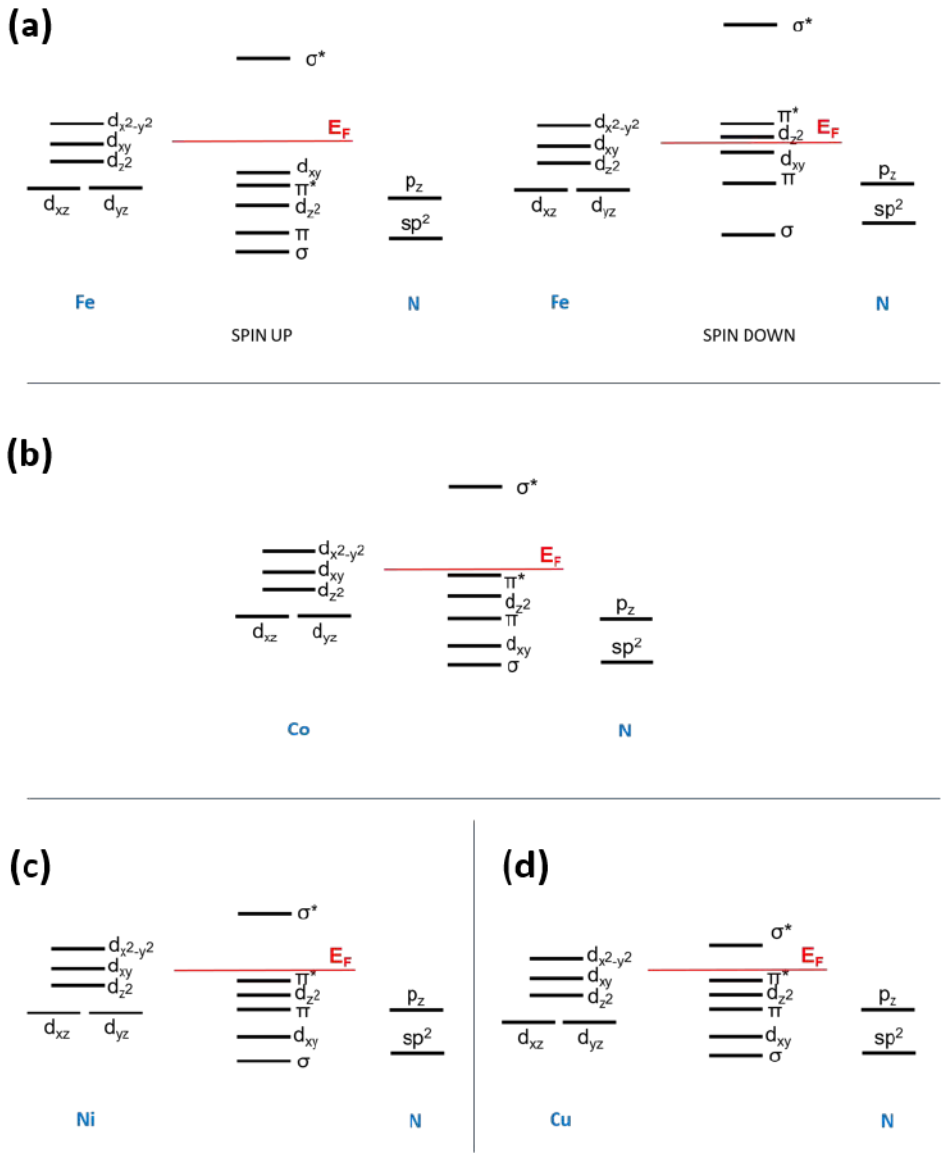

Figure 7: MO diagrams of free-standing N-doped (a) Fe@4N2VG, (b) Co@4N2VG, (c) Ni@4N2VG, and (d) Cu@4N2VG. Relative position of the levels is derived from the PDOS in Figure 8.

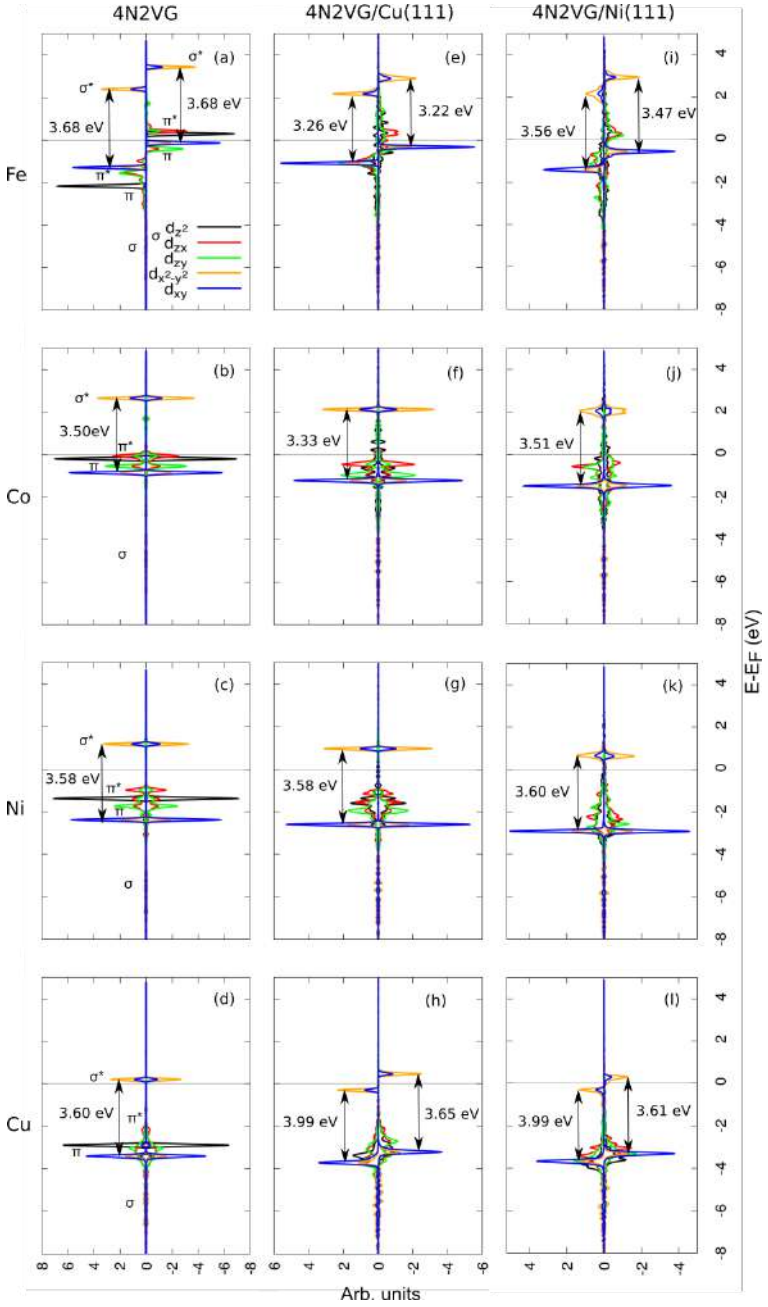

Figure 8: PDOS on the d-states of the transition metal adatom in free-standing nitrogen-doped (a) Fe@4N2VG, (b) Co@4N2VG, (c) Ni@4N2VG, (d) Cu@4N2VG, and supported (e) Fe@4N2VG/Cu(111), (f) Co@4N2VG/Cu(111), (g) Ni@4N2VG/Cu(111), (h) Cu@4N2VG/Cu(111), (i) Fe@4N2VG/Ni(111), (j) Co@4N2VG/Ni(111), (k) Ni@4N2VG/Ni(111), and (l) Cu@4N2VG/Ni(111).

On the strongly interacting Ni(111) instead the TMs are much closer to the surface than in the case of Cu(111), as evident from the side views. The symmetry of the square-planar geometries on Ni(111) are not as perfect as on Cu(111) but far better than the free-standing ones for Co@2VG and Fe@2VG.

The buckling of the graphene layer is around 0.15 Å which is definitely smaller than it was on Cu(111) (1 Å).

In the following, we discuss the effect of the metal substrates on the electronic structure of the supported TM@2VG layers. The case of TM@2VG systems on the Cu(111) are shown in Figures 4(e-h). The analysis is based on the MO-diagrams of the corresponding free-standing cases given in Figure 3. We start from Fe@2VG/Cu(111), which is the only TM atom retaining some spin-polarization, even though the magnetic moment is reduced with respect to the free-standing Fe@2VG. The first major difference is the disappearance of the d_z^2 peak in the PDOS (see Figure 4(e)). This is due to the presence of the Cu substrate whose surface states mix up with the d_z^2 thereby making it greatly dispersed. A similar broadening effect is observed also for the π and π* orbitals. The next difference is in the separation between the d_{xy} and the σ* peaks, which has decreased from 6.01 eV, in the case of Fe@2VG, to 4.75 eV in the case of Fe@2VG/Cu(111). This is due to the presence of the underlying Cu substrate and its effect on the magnetization of the Fe adatom. Finally, the spin-down d_{xy} is found at the Fermi level.

When Co@2VG is supported on the Cu(111), the magnetic character of the system is quenched (see Figures 4(b and f)) and the separation between the d_{xy} and σ* peaks is reduced by 0.94 eV. This value was 1.26 eV in the case of Fe@2VG/Cu(111). Therefore, the impact of the Cu substrate potential is slightly less on Co than it was on Fe. There is quite a lot of d-orbital mixing of Co with the surface states, similar to what we observed for Fe@2VG/Cu(111).

In the case of Ni@2VG/Cu(111), the system is very similar to Co@2VG/Cu(111) (see Figure 4, third vs second line), except that the Fermi energy has slightly moved closer to the σ* in the former and, the d_{xy} in Ni@2VG/Cu(111) is taller and hence less dispersed than that in Co@2VG/Cu(111). While comparing with the free-standing Ni@2VG, the (d_{xy} - σ*) energy separation in Ni@2VG/Cu(111) has decreased by half an eV, which indicates an influence of the potential of the Cu substrate on the Ni adatom, which is however smaller than what it was on Co and Fe.

Last but not the least, Cu@2VG/Cu(111) is quite different from Ni@2VG/Cu(111) and Co@2VG/Cu(111) (Figure 4, fourth vs second and third) since we observe huge orbital mixing and dispersion for all the d-states. The (d_{xy} - σ*) separation is the largest among all the Cu(111) supported cases and only 0.28 eV smaller than its respective free-standing Cu@2VG case. Hence, the influence of the Cu substrate potential manifests to be minimal here among all the other cases. Other than that, the d_z^2 appears before the d_{xy} (different from its free-standing counterpart) and the Fermi level appears the closest to σ* in this particular case. As a trend, we observe that going from Fe, to Co, Ni and Cu, σ* gets closer to the Fermi level of the systems, as the d states are progressively deeper in energy.

Moving from the Cu(111) to the Ni(111) substrate, since the TM@2VG layer gets much closer to the metal surface with the adsorption distance shortening by more than one Å, one would expect the orbitals with out-of-plane character, such as the π and π*, to undergo much more mixing and interaction with the surface states. This is indeed true, as we can observe in Figures 4(i-l). In general, the black, the red and the green curves, corresponding to d_z^2, d_{zx} and $d_{zy,}$ are much more dispersed and spread on Ni(111) than on Cu(111).

In the case of Fe@2VG on Ni(111), the magnetic character of Fe is almost totally quenched and the (d_{xy} - σ*) separation is further lowered by 0.15 eV with respect to Fe@2VG on Cu(111). On the other hand, some magnetic character is maintained in Co@2VG/Ni(111), similar to the free-standing Co@2VG, which was otherwise fully quenched on Cu(111). In the case of Co, Ni and Cu, the (d_{xy} - σ*) separation is much less affected by the presence of the substrate. In particular and very interestingly, the values of the (d_{xy} - σ*) separation of Cu@2VG/Cu(111) and Ni@2VG/Ni(111), which remain very similar to the corresponding free-standing ones (see Figures 4(c,k) and 4(d,h)); i.e. the substrate potential felt by the TM is the smallest when the TM adatom is of the same species as that of the substrate

3.4.2 Fe, Co, Ni, Cu @ N-doped G on Cu(111) and Ni(111)

In this section we present the N-doped systems deposited on the Cu(111) and Ni(111) substrates. The TM@3N1VG systems can present the TM atom positioned at the top or fcc adsorption sites of the (111) face of the metal substrates. We start by examining the structures on the Cu(111). The optimized configurations obtained for TM@3N1VG/Cu(111) at the top site are shown in Figures 5(e-h), whereas those at the fcc site in Figures 5(i-l). At the top site, the TM atom is found to form a bond with the Cu atom of the substrate lying directly below, exactly like in the TM@1VG/Cu(111) case (see Figures 1(e-h)). However, the situation is quite different for the fcc sites of Figures 5(i-k). Here a bond between one of the three N atoms and the Cu substrate is established, except for the TM Cu. In that case (Figure 5(l)), the Cu atom is out of the graphene plane together with the coordinating N atoms on the opposite side with respect to the substrate. The fcc site is preferred to the top site for Fe@3N1VG/Cu(111), Co@3N1VG/Cu(111), Ni@3N1VG/Cu(111), and Cu@3N1VG/Cu(111) by 2.29 eV, 2.10 eV, 2.04 eV, and 1.68 eV, respectively. The lower value for Cu@3N1VG/Cu(111) is due to the difference in its structure.

The behavior of the TM on Ni(111) seems structurally to be more regular in fashion. At the top sites all the TM in TM@3N1VG/Ni(111) are pushed away from the substrate, together with the N atoms attached to them (see Figures 5(m-p)). Whereas at the Ni(111) fcc sites the TM atoms are drawn in towards the substrate. Energy wise, for Fe@3N1VG/Ni(111), Co@3N1VG/Ni(111), Ni@3N1VG/Ni(111) and Cu@3N1VG/Ni(111) the fcc sites are favored than the top sites by 1.17 eV, 1.09 eV, 1.06 eV and 0.82 eV, respectively.

Next, we discuss the effect of the metal substrates in the TM trapped at the N-doped double vacancies or TM@4N2VG systems, whose optimized geometries are shown in Figures 6(e-h) and the structural parameters are reported in Table 2. All of them are found to exhibit quite regular square-planar structures. As the registry of G with the two metal substrates considered here is top-fcc, at the 2VG the two absent C atoms are from the consecutive top and fcc sites. Hence, the adsorption site of the TM atom in the 2VG is exactly in the middle of those top and fcc sites. In the case of Fe@4N2VG/Cu(111) and Co@4N2VG/Cu(111), the TM forms bonds with the top site Cu atom underneath in Figures 6(e and f), with Fe being the closest to the substrate (2.54 Å). Different is the case for Ni@4N2VG/Cu(111) and Cu@4N2VG/Cu(111), where Ni and Cu lie in the G plane in Figures 6(g and h). Next, on Ni(111) the square-planar structures are not as symmetric as on Cu(111), which could be due to the stronger interaction of G with the former (see Table 2). The Fe atom is found to bind with three of the top site Ni substrate atoms as in Figure 6(i) and is as close as 2.14 Å to the substrate. The Co, Ni and Cu adatoms are found to form bond with only the top site Ni substrate atom underneath (see Figures 6(j-l)).

The density of states of TM@4N2VG/Cu(111) are shown in Figure 8(e-h), which can be corroborated by means of the MO diagrams of the corresponding free-standing systems of Figures 7. For all the four TM we notice that the σ/σ* states are large downward shifted with respect to the Fermi level with respect to the corresponding structures in Figure 4 where N was not present. As discussed above, this is because the N sp^2 and p states are deeper than the C sp^2 and p states.

The PDOS of Fe@4N2VG/Cu(111) is shown in Figure 8(e), where the orbitals with some z character, i.e. d_{z2} (black), d_{zx} (red) and d_{zy} (green curves), are heavily dispersed and spread over a larger energy range compared to those of the free-standing Fe@4N2VG (see Figure 8(a)). The (d_{xy} - σ*)

separation is 1.49 eV smaller than its non-N-doped counterpart, Fe@2VG/Cu(111) of Figure 4(e). This is because, looking at the spin-up component, the σ* in Fe@4N2VG/Cu(111) has shifted by almost this same amount towards the Fermi level (hence towards the d_{xy}), than in Fe@2VG/Cu(111), thereby reducing the gap. This is the result of the deeper position of the N states involved in the σ/σ* orbitals.

The PDOS of Co@4N2VG/Cu(111) is shown next in Figure 8(f). The σ* has moved nearer to the Fermi level by almost 2 eV than it was in the non-N-doped Co@2VG/Cu(111) (see Figure 4(f)), thereby also reducing the (d_{xy} - σ*) separation by 1.23 eV. This again showcases the role of the four electron rich N atoms making bonds with Co. Comparing with its free-standing counterpart Co@4N2VG, in Co@4N2VG/Cu(111) the (d_{xy} - σ*) separation has reduced by 0.17 eV, which is due to the influence of the Cu(111) substrate potential, whereas in Ni@4N2VG/Cu(111) it remains more or less similar as for Ni@4N2VG. This separation is 1.28 eV smaller than for Ni@2VG/Cu(111). The σ* has shifted much closer to the Fermi level (almost by 3 eV) than the non-N-doped case (see Figure 4(g)), stimulated by the orbital splitting due to the bond formation with N. In the case of Cu@4N2VG/Cu(111), some spin-polarization has appeared, which was otherwise absent in the free-standing Cu@4N2VG. Moreover, for the first time in this study, we observe that the σ* in the spin-up component is completely filled and below the Fermi level for Cu@4N2VG/Cu(111). The reduction in the (d_{xy} - σ*) separation is the highest, of 1.64 eV compared to Cu@2VG/Cu(111).

Next we investigate what happens to the N-doped TM@4N2VG supported on Ni(111). Fe remains spin-polarized also on Ni(111), as seen in Figures 8(a, e, and i), with a (d_{xy} - σ*) separation close to that for free-standing. We can observe that Fe@2VG/Ni(111) was non-magnetic whereas Fe@4N2VG/Ni(111) has a magnetism of 1.38 μB (see Tables 1 and 2). Hence, we can conclude that this induced magnetism is due to the bonds with the N-atoms alone. For both Co@4N2VG/Ni(111) and Ni@4N2VG/Ni(111) the (d_{xy} - σ*) separation remains very similar to both the free-standing Cu(111) and supported cases, as seen in Figures 8(b, f, j) and 8(c, g, k). In the case of Co@4N2VG/Ni(111), the magnetism, which was present in the non-N-doped Co@2VG/Ni(111), has been quenched due to the bond with the four neighboring N atoms. In the case of Cu@4N2VG/Ni(111), a magnetism of 0.38 μB has been induced compared to the non-magnetic non-N-doped Cu@2VG/Ni(111). The σ* of the spin-up component of Cu@4N2VG/Ni(111) gets completely filled, like in the case of Cu@4N2VG/Cu(111).

3.5 Comparative analysis of energetics

In this section, several aspects of the energetics of these systems will be discussed. We will restrict the analysis to the systems where the TM is trapped at non-N-doped and N-doped double vacancies, for two reasons: 1) 2VG is a better suited host in terms of the available space for large TM atoms and 2) 2VGs are more commonly present and stable than the 1VGs according to experiments.[17]

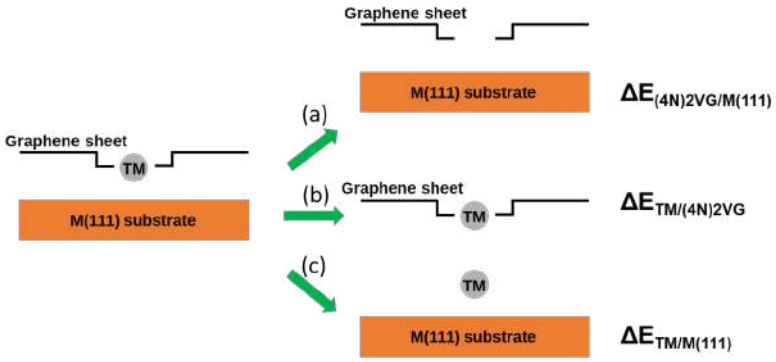

Figure 9: The interaction energies in TM@(4N)2VG/M(111) can be broken down into three parts: (a) $\Delta E_{(4N)2VG/M(111)} = E_{(4N)2VG/M(111)frozen} - E_{(4N)2VGfrozen} - E_{M(111)frozen}$, (b) $\Delta E_{TM/(4N)2VG} = E_{TM@(4N)2VGfrozen} - E_{(4N)2VGfrozen} - E_{TM}$, (c) $\Delta E_{TM/M(111)} = E_{TM/M(111)frozen} - E_{M(111)frozen} - E_{TM}$.

In Figure 9 we define three components of the interaction energy in these multicomponent systems, i.e. TM@2VG/M(111) and TM@4N2VG/M(111). They are computed by keeping the fragments frozen at the optimized final geometry for the overall TM@2VG/M(111) and TM@4N2VG/M(111) systems, shown in Figures 2(e-l) and 6(e-l), respectively. This means that the energy required for any kind of structural deformation or distortion is not included in this type of analysis, but rather we evaluate only the electronic interactions between the different fragments of these systems. As can be seen in the Figure 9, the three components of the interaction energies in TM@2VG/M(111) are: (a) $\Delta E_{2VG/M(111)}$ between the 2VG monolayer sheet and the M(111) substrate, (b) $\Delta E_{TM/2VG}$ between the TM adatom and the 2VG sheet, and (c) $\Delta E_{TM/M(111)}$ between the TM adatom and the M(111) substrate. The part of the system not of interest was simply removed keeping the rest of it intact. For example, (a) is computed as $\Delta E_{2VG/M(111)} = E_{2VG/M(111)frozen} - E_{2VGfrozen} - E_{M(111)frozen}$, where $E_{2VG/M(111)frozen}$ is the total energy of 2VG/M(111) after removing the TM, $E_{2VGfrozen}$ is the total energy of 2VG without TM and $E_{M(111)frozen}$ is the total energy of M(111) all with the coordinates fixed as in the final geometry (see Figures 2(e-l) for the optimized geometries), i.e. single point calculations were run in the absence of TM. Similarly, these

energies have been computed also for the N-doped systems by simply replacing the 2VG energy with the N-doped 4N2VG one, as will be discussed later. The values for all the contributions are reported in Table 3. We will first discuss the non-N doped systems.

Table 3: The values of the interaction energies in "eV" of TM@(4N)2VG/M(111), i.e. (a) $\Delta E_{(4N)2VG/M(111)}$, (b) $\Delta E_{TM/(4N)2VG}$, and (c) $\Delta E_{TM/M(111)}$ depicted in Figure 9 are given here. The values obtained for the N-doped systems are given in brackets.

On Cu(111)	(a) $\Delta E_{(4N)2VG/M(111)}$	(b) $\Delta E_{TM/(4N)2VG}$	(c) $\Delta E_{TM/M(111)}$
Fe@2VG (Fe@4N2VG)	-6.41 (-4.04)	-10.20 (-8.36)	-1.98 (-2.49)
Co@2VG (Co@4N2VG)	-6.45 (-3.87)	-10.50 (-8.97)	-2.77 (-2.06)
Ni@2VG (Ni@4N2VG)	-6.55 (-3.68)	-10.60 (-8.90)	-3.34 (-1.19)
Cu@2VG (Cu@4N2VG)	-5.99 (-3.67)	-8.98 (-5.92)	-2.58 (-1.31)
On Ni(111)	**(a) $\Delta E_{(4N)2VG/M(111)}$**	**(b) $\Delta E_{TM/(4N)2VG}$**	**(c) $\Delta E_{TM/M(111)}$**
Fe@2VG (Fe@4N2VG)	-11.23 (-9.39)	-9.42 (-8.19)	-3.96 (-3.64)
Co@2VG (Co@4N2VG)	-11.36 (-9.39)	-9.89 (-8.91)	-4.19 (-3.13)
Ni@2VG (Ni@4N2VG)	-11.29 (-9.39)	-10.01 (-8.69)	-3.30 (-2.64)
Cu@2VG (Cu@4N2VG)	-10.67 (-9.54)	-8.36 (-5.77)	-2.09 (-2.43)

On both Cu(111) and Ni(111), Cu@2VG/M(111) is characterized by the least negative values for the (a) and (b) components of the interaction energy, which agrees with the observed lowest buckling of the graphene layer. On Cu(111) the interaction energy component (a) between the 2VG sheet and M(111) substrate is the strongest for Ni@2VG/Cu(111) while on Ni(111) the strongest is in Co@2VG/Ni(111). This is due to the fact that the buckling in the graphene layer caused by the Ni adatom is the highest among all the TMs on Cu(111) and by Co on Ni(111) (see Table 1).

The interaction energy component (b) between the TM and the 2VG sheet, computed as $\Delta E_{TM/2VG} = E_{TM@2VGfrozen} - E_{2VGfrozen} - E_{TM}$, where the last term is the energy of a free TM atom, follows the same trend as (a) on Cu(111) going from the most negative to the less negative: Ni, Co, Fe, and Cu. The same is true also on Ni(111). The last interaction energy component (c) between the TM adatom and

the metal substrate is computed as $\Delta E_{TM/M(111)} = E_{TM/M(111)frozen} - E_{M(111)frozen} - E_{TM}$, where $E_{TM/M(111)frozen}$ is the total energy of the TM/M(111) system without the C atoms and the coordinates fixed as in the final geometry. The strongest to the weakest interaction of the TMs with Cu(111) is in the order Ni, Co, Cu, Fe, whereas with Ni(111) is Co, Fe, Ni and Cu.

In the N-doped cases on Cu(111), the most negative value of (a) or $\Delta E_{4N2VG/M(111)}$ is obtained for Fe@4N2VG/Cu(111), which is in-line with the observed highest level of buckling induced in graphene, among all the TMs. Whereas Ni and Cu TMs induce the lowest buckling in graphene thereby resulting in the least negative energy values obtained. On Ni(111), Fe, Co, and Ni give similar values for (a) in accordance with the similar values of buckling of the graphene layer (see Table 2). The interaction energy (b) or $\Delta E_{TM/4N2VG}$ for the N-doped systems gives a measure of the interaction strength of the TM atom with the four N atoms of the graphene layer. Both on Cu(111) and Ni(111), this is the strongest for Co and Ni, followed by Fe and the least for Cu. The last energy term (c) or $\Delta E_{TM/M(111)}$ i.e. the interaction of the TMs with the Cu(111) substrate is computed in the same way as for the non-N-doped cases. The interaction strength from the strongest to the weakest is Fe, Co, Cu, Ni, both on Cu(111) and Ni(111), which is completely different from that of the cases without N-doping, due to the different height of the TM atom (see Table 2): the strongest interacting Fe is the closest to the substrate surface and the least interacting Ni is the farthest.

In Figure 10(a) we discuss the deformation $\Delta E_{deformation}$, bond ΔE_{bond} and adsorption $\Delta E_{adsorption}$ energies. The deformation energy is defined as $\Delta E_{deformation} = E_{M(111)frozen} - E_{M(111)} + E_{(4N)2VGfrozen} - E_{(4N)2VG}$, where $E_{M(111)frozen}$ is the energy of the deformed metal substrate and $E_{(4N)2VGfrozen}$ is the energy of the deformed (4N)2VG sheet, both with the coordinates frozen as in the optimized TM@(4N)2VG/M(111) geometry. $E_{M(111)}$ is the energy of the relaxed pristine metal substrate and $E_{(4N)2VG}$ is the energy of the relaxed free-standing (4N)2VG sheet (see Figure S2(b and d) for optimized structures). Thus, $\Delta E_{deformation}$ takes into account the energy required to structurally deform both the (4N)2VG sheet and the M(111) substrate into their final geometry in the optimized TM@(4N)2VG/M(111). The values of which are given in Table 4. As we can see, the deformation energies are always positive for all the systems.

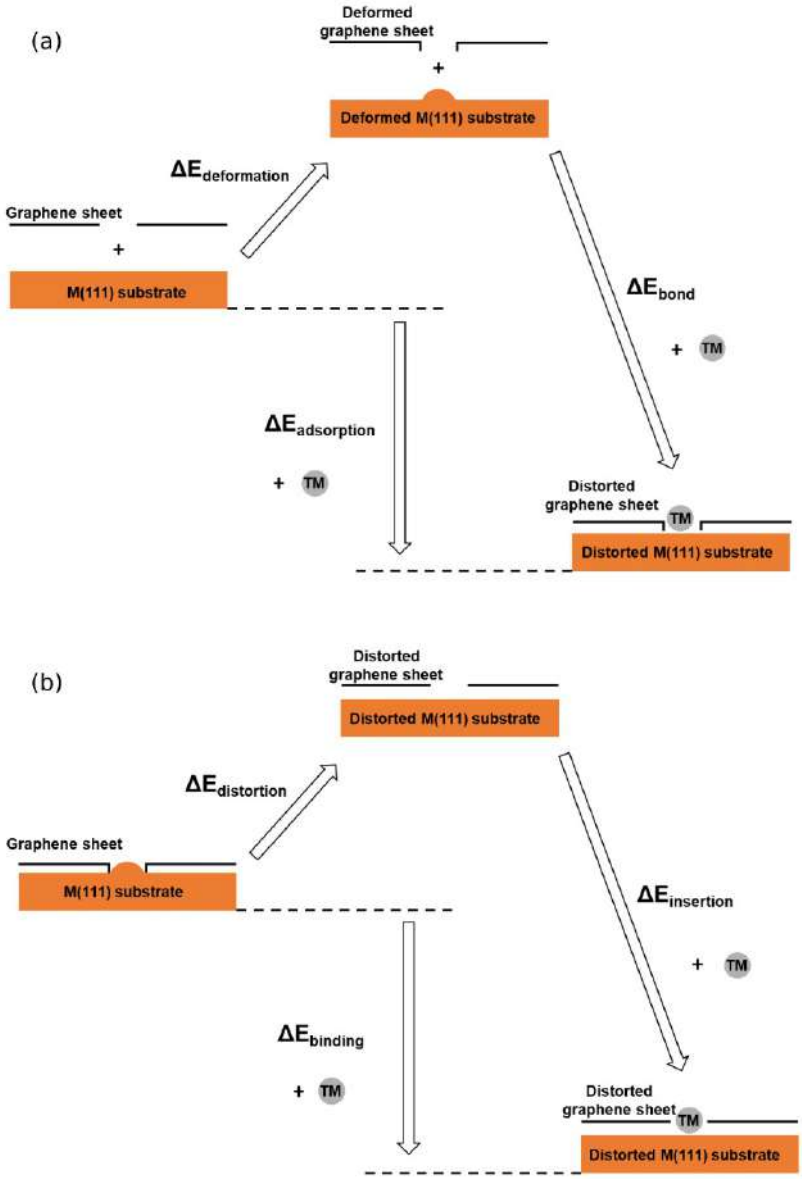

Figure 10: Energy decomposition analysis. (a) $\Delta E_{deformation} = E_{M(111)frozen} - E_{M(111)} + E_{(4N)2VGfrozen} - E_{(4N)2VG}$, $\Delta E_{bond} = E_{TM@(4N)2VG/M(111)} - E_{M(111)frozen} - E_{(4N)2VGfrozen} - E_{TM}$, $\Delta E_{adsorption} = E_{TM@(4N)2VG/M(111)} - E_{M(111)} - E_{(4N)2VG} - E_{TM}$. (b) We call the energy required for distorting the G/TM(111) in order to accommodate the TM adatom as the distortion energy which is a positive value, $\Delta E_{distortion} = E_{(4N)2VG/M(111)frozen} - E_{(4N)2VG/M(111)}$. This is then stabilized enormously just by the insertion of the TM adatom into the frozen geometry, here represented by the insertion energy, $\Delta E_{insertion} = E_{TM@(4N)2VG/M(111)} - E_{(4N)2VG/M(111)frozen} - E_{TM}$. Whereas the binding energy is the energy needed for binding the TM adatom to the pristine (4N)2VG/M(111), $\Delta E_{binding} = E_{TM@(4N)2VG/M(111)} - E_{(4N)2VG/M(111)} - E_{TM}$.

For the non-N-doped systems on Cu(111), the Fe@2VG exhibits the highest $\Delta E_{deformation}$ followed by Co@2VG, Ni@2VG and Cu@2VG. This trend is in accordance with the displacement of the TMs towards the substrate with Fe being the closest at a height of 1.89 Å from the Cu(111) surface (with respect to

the average height of the first layer Cu atoms) as reported in Table 1. Co, Ni and Cu are at 1.94, 2.08 and 2.24 Å, respectively. We remark that on Cu(111) the graphene layer is around 3 Å high and hence all the TMs are found more or less around 1 Å below the plane of the 2VG towards the substrate. This appreciable displacement is the reason for the deformation in 2VG and Cu(111) substrate costing about 4 eV for all the TM@2VG/Cu(111) systems. This is not the case on Ni(111) as all the deformation energies are much lower, around 1.2 eV (see Table 4). Graphene is 1 Å closer on Ni(111) than on Cu(111), as reported in Table 1. Hence, on Ni(111) the most displaced TM atom (Fe) from the graphene layer is only 0.5 Å below the 2VG, followed by Co, Ni and Cu, which practically lies in the plane of graphene. Therefore, also the deformation in 2VG and Ni(111) (caused by the TM) is less compared to that on Cu(111).

In the case of N-doped systems, there is a huge difference in the values of deformation energy. For the Cu(111) supported cases, $\Delta E_{deformation}$ is five times smaller for Fe@4N2VG than Fe@2VG, while for Cu@4N2VG it is ten times smaller than Cu@2VG. This is directly related to the buckling of the graphene layer which is two to ten orders smaller for TM@4N2VG/Cu(111) than TM@2VG/Cu(111). Hence, we remark that the major contribution (almost 90%) towards the $\Delta E_{deformation}$ is mainly due to the deformation of the graphene layer rather than that of the Cu(111) substrate. On the strongly interacting Ni(111) support, instead, the buckling of the graphene layer (considering the C atoms alone) itself has not changed much from TM@2VG/Ni(111) to TM@4N2VG/Ni(111). But if you consider also the N atoms present, the buckling has increased (see buckling of N-doped G on Ni(111) in Table 2), thence the $\Delta E_{deformation}$ is slightly higher on TM@4N2VG/Ni(111) than on TM@4N2VG/Cu(111). However, the deformation energy on Ni(111) has reduced by three to four orders of magnitude for the N-doped ones than the non-N-doped ones, suggesting that N-doping has brought better stability to the structures.

The bond energy in Figure 10(a) is defined as $\Delta E_{bond} = E_{TM@(4N)2VG/M(111)} - E_{M(111)frozen} - E_{(4N)2VGfrozen} - E_{TM}$, where $E_{TM@(4N)2VG/M(111)}$ is the total energy of the system in the final optimized geometry, $E_{M(111)frozen}$ is the energy of the deformed metal substrate, $E_{(4N)2VGfrozen}$ is the energy of the deformed (4N)2VG sheet, both with the coordinates frozen as in the optimized TM@(4N)2VG/M(111) geometry. E_{TM} is the energy of the isolated TM atom. Hence, ΔE_{bond} gives us the energy required for bonding the TM atom to the (4N)2VG and M(111) in the final geometry. The values of ΔE_{bond} on Cu(111) and Ni(111) are given in Table 4. For TM@2VG/Cu(111), the most stable bond energy is obtained for Co and the least for Cu, whereas on Ni(111) they are Co and Cu, respectively. Ditto in the case of their N-doped counterparts.

The adsorption energy in Figure 10(a) is computed as $\Delta E_{adsorption} = E_{TM@(4N)2VG/M(111)} - E_{M(111)} - E_{(4N)2VG} - E_{TM}$, where all the terms have been defined previously. The only difference between $\Delta E_{adsorption}$ and

ΔE_{bond} being that the former is computed with respect to the relaxed free-standing (4N)2VG sheet and pristine M(111) substrate whereas the latter is computed with respect to frozen (4N)2VG and M(111). Both Cu(111) and Ni(111) supported structures show the same trend as for $\Delta E_{adsorption}$, with the most stably adsorbed being Co, followed by Ni, Fe and finally Cu. In the case of TM@4N2VG/M(111), there is a switch between Ni and Fe in the order of stability, the rest remaining the same.

Table 4: Adsorption energy $\Delta E_{adsorption}$, bond energy ΔE_{bond} and deformation energy $\Delta E_{deformation}$ in "eV". The values obtained for the N-doped systems are given in brackets.

On Cu(111)	$\Delta E_{adsorption}$	ΔE_{bond}	$\Delta E_{deformation}$
Fe@2VG (Fe@4N2VG)	-12.15 (-12.28)	-17.10 (-13.21)	4.95 (0.93)
Co@2VG (Co@4N2VG)	-12.76 (-12.79)	-17.65 (-13.56)	4.89 (0.76)
Ni@2VG (Ni@4N2VG)	-12.65 (-12.12)	-17.34 (-12.75)	4.69 (0.64)
Cu@2VG (Cu@4N2VG)	-10.25 (-9.33)	-14.55 (-9.77)	4.30 (0.44)
On Ni(111)	**$\Delta E_{adsorption}$**	**ΔE_{bond}**	**$\Delta E_{deformation}$**
Fe@2VG (Fe@4N2VG)	-17.99 (-16.69)	-21.68 (-17.61)	3.69 (0.93)
Co@2VG (Co@4N2VG)	-18.54 (-17.11)	-22.10 (-18.09)	3.56 (0.99)
Ni@2VG (Ni@4N2VG)	-18.21 (-16.21)	-21.58 (-17.41)	3.37 (1.20)
Cu@2VG (Cu@4N2VG)	-15.94 (-13.46)	-19.12 (-14.55)	3.18 (1.09)

In Figure 10(b) we investigate the distortion $\Delta E_{distortion}$, binding $\Delta E_{binding}$ and insertion $\Delta E_{insertion}$ energies. The values of these terms, for both Cu(111) and Ni(111) substrates, are reported in Table 5. The distortion energy is calculated as $\Delta E_{distortion} = E_{(4N)2VG/M(111)frozen} - E_{(4N)2VG/M(111)}$, where $E_{(4N)2VG/M(111)frozen}$ is the total energy of the (4N)2VG/M(111) in the final TM@(4N)2VG/M(111) geometry without the TM atom and $E_{(4N)2VG/M(111)}$ is the total energy of the optimized empty (N-doped) double vacancy G adsorbed on M(111) (see Figure S3 (d and h) for non-N-doped and Figure S4 (c and f) for N-doped optimized geometries). The distortion energy is the counterpart of the deformation energy when the two units (4N)2VG and M(111) are bonded together. In other words, it is the distortion occurring in the (4N)2VG/M(111) system when considered as a single unit. Similar to the case of deformation energy also the $\Delta E_{distortion}$ on Ni(111) is around 1 eV smaller than on Cu(111). This is because of the difference in the adsorption heights of G in the two systems. The highest distortion energy is found for Fe@2VG

on Cu(111) followed by Co@2VG, Cu@2VG and Ni@2VG. On Ni(111) instead the highest value is found for Cu@2VG followed by Fe@2VG, Co@2VG and Ni@2VG. As one can see from Table 5, for the N-doped cases, the $\Delta E_{distortion}$ is almost ten orders of magnitude smaller on Cu(111) and four orders of magnitude smaller on Ni(111) with respect to the respective non-N-doped ones. The reason for this remarkable difference is as follows. First of all if we compare the optimized geometries of the reference systems on Cu(111), i.e. 2VG/Cu(111) of Figure S3(d) and 4N2VG/Cu(111) of Figure S4(c), there is a huge difference between them. In the former the dangling bonds at the empty 2VG is so strongly interacting with Cu(111) that one of the substrate atoms is pulled out of the substrate, hence heavily distorting the graphene layer. While in the latter, when the N atoms are present at the double vacancy, this is not the case. On the other hand, for TM@4N2VG/Ni(111), the $\Delta E_{distortion}$ is almost twice of that for TM@4N2VG/Cu(111) due to the higher buckling of N-doped G in the former (see Table 2).

Table 5: Binding energy $\Delta E_{binding}$, insertion energy $\Delta E_{insertion}$ and distortion energy $\Delta E_{distortion}$ in "eV". The values obtained for the N-doped systems are given in brackets.

On Cu(111)	$\Delta E_{binding}$	$\Delta E_{insertion}$	$\Delta E_{distortion}$
Fe@2VG (Fe@4N2VG)	-6.07 (-8.68)	-10.70 (-9.17)	4.62 (0.48)
Co@2VG (Co@4N2VG)	-6.68 (-9.20)	-11.10 (-9.68)	4.43 (0.48)
Ni@2VG (Ni@4N2VG)	-6.57 (-8.53)	-10.90 (-9.07)	4.32 (0.55)
Cu@2VG (Cu@4N2VG)	-4.17 (-5.74)	-8.56 (-6.11)	4.39 (0.37)
On Ni(111)	**$\Delta E_{binding}$**	**$\Delta E_{insertion}$**	**$\Delta E_{distortion}$**
Fe@2VG (Fe@4N2VG)	-6.81 (-7.39)	-10.45 (-8.22)	3.64 (0.83)
Co@2VG (Co@4N2VG)	-7.36 (-7.81)	-10.74 (-8.71)	3.37 (0.90)
Ni@2VG (Ni@4N2VG)	-7.03 (-6.91)	-10.29 (-8.02)	3.26 (1.10)
Cu@2VG (Cu@4N2VG)	-4.76 (-4.16)	-8.45 (-5.01)	3.68 (0.85)

The binding energy is instead determined as $\Delta E_{binding} = E_{TM@2VG/M(111)} - E_{2VG/M(111)} - E_{TM}$, where all the terms are as already defined. The values for both Cu(111) and Ni(111) are reported in Table 5. Hence, this energy defines the adsorption of the TM atom to fill the otherwise empty 2VG/M(111) in its relaxed configuration. The most stable binding energy among the four TM@2VG/Cu(111) is Co@2VG, followed

by Ni@2VG, Fe@2VG and Cu@2VG. The behavior is the same on Ni(111) i.e. in the order from the most to the least stable: Co@2VG, Ni@2VG, Fe@2VG and Cu@2VG. In Table 5 the binding energy of the N-doped systems on Cu(111) and on Ni(111) are also provided in brackets. This quantity is calculated as $E_{TM@4N2VG/M(111)} - E_{4N2VG/M(111)} - E_{TM}$. We can see that the binding energy of Fe@4N2VG/Cu(111) is 2.53 eV more stable than that of Fe@2VG/Cu(111). Similarly the other systems containing Co, Ni and Cu as TM on Cu(111) exhibits binding energies less stable than for their N-doped counterparts by 2.29 eV, 1.99 eV and 1.55 eV, respectively. On Ni(111), we do not observe such different behavior: Fe and Co are less stable than their N-doped counterparts by only 0.58 eV and 0.45 eV, respectively. Instead Ni and Cu TM@2VG/Cu(111) are more stable than their corresponding N-doped systems by only 0.12 eV and 0.60 eV, respectively. As we often mention, Ni(111) is a strongly interacting support, therefore, it is less sensitive to chemically different graphene layers.

The last energy of interest is the insertion energy, which is $\Delta E_{insertion} = E_{TM@(4N)2VG/M(111)} - E_{(4N)2VG/M(111)frozen} - E_{TM}$. Therefore, the only difference with respect to $\Delta E_{binding}$ is that the energy of the (4N)2VG/M(111) in the frozen final optimized geometry in TM@(4N)2VG/M(111) is considered. In other words $\Delta E_{insertion}$ is the energy lost or gained in order to insert the isolated TM atom into the (4N)2VG/M(111) when the coordinates are fixed as in the optimized final TM@(4N)2VG/M(111) structure. Here, for the non-N-doped cases, the most stable one on Cu(111) is always Co@2VG. The next stable ones are Ni, Fe, and Cu. On Ni(111) the order is slightly different, the most to the least stable ones are Co@2VG, Fe@2VG, Ni@2VG, and Cu@2VG. For the N-doped cases, Co@4N2VG/Cu(111) is the most stable one, followed by Fe@4N2VG/Cu(111), Ni@4N2VG/Cu(111) and Cu@4N2VG/Cu(111). Whereas on Ni(111), the stability order is the same as the non-N-doped cases.

In this section we have discussed in detail the energetics of the SAC atoms trapped in defects of free-standing and supported graphene, however we have not discussed the kinetics of migration of these TM atoms as it has been already investigated in previous studies, where both static and dynamic calculations clearly indicated that they are immobile up to very high temperatures, even in the presence of an underlying metal substrate.[39-41]

3.6 Hydrogen Evolution Reaction (HER) at SACs trapped in defective graphene: role of N-dopants and of the metal substrate

The activity of the SACs towards HER was studied by adsorbing atomic H at the TM atom in the TM@(4N)2VG free-standing as well as the supported systems. The computed Gibb's free energy for atomic H adsorption (ΔG_{H^*}), which is the best descriptor of HER activity, is reported in Table 6 (see Methods section for more details). The H atom was positioned on top of the TM in all the initial configurations and optimized to obtain the final configurations when free-standing (Figure S7), supported on Cu(111) (Figure S8) or on Ni(111) (Figure S9). We would like to remark that only in the particular case of free-standing Cu@2VG, even though in the initial configuration the H atom was positioned on the Cu, it moved onto the neighbouring C atom in the optimized final geometry (see Figure S7(d)). This suggests that H adsorption is not favoured on Cu. Given that the closer the ΔG_{H^*} is to zero (isoenergetic step), the better the HER performance of the catalyst, we observe that, upon N-doping of graphene, trapped Fe and Co improve whereas Ni and Cu (with the H atom now adsorbed on Cu) worsen.

When adsorbed on Cu(111) and on Ni(111), the ΔG_{H^*} values for Fe@2VG and Co@2VG are observed to improve compared to their free-standing counterparts. For Ni@2VG/Cu(111) and Ni@2VG/Ni(111) the situation remains similar to Ni@2VG, and Cu@2VG/Cu(111) is worst among the four. N-doping has a negative effect on the catalytic activity of the supported systems. This is because the binding energy between TM and the defective graphene (see Table 5) increases through N interposition, thereby reducing the TM binding with H.

Concluding, the best candidates for HER catalysis among the ones considered in this study are Co-containing systems, in particular free-standing Co@4N2VG and supported Co@2VG/Ni(111).

Table 6: Gibb's free energy for hydrogen adsorption (ΔG_{H^*}) on the TM in "eV". The values obtained for the N-doped systems are given in brackets. For optimized geometries see Figures S7, S8 and S9 in the Supplementary Information. *In Cu@2VG the H atom does not adsorb on the Cu but the neighboring C atom.

ΔG_{H^*}	Free-standing	On Cu(111)	On Ni(111)
Fe@2VG (Fe@4N2VG)	0.38 (0.19)	0.18 (0.70)	0.21 (0.73)
Co@2VG (Co@4N2VG)	0.22 (0.12)	0.19 (0.53)	0.13 (0.76)
Ni@2VG (Ni@4N2VG)	0.44 (1.67)	0.48 (1.65)	0.40 (1.59)
Cu@2VG* (Cu@4N2VG)	-0.16* (1.75)	1.26 (1.90)	1.17 (1.54)

4. Conclusions

In this work we have presented a systematic and comparative investigation of the structural, electronic and energetics properties of several transition metal atoms of the first raw (Fe, Co, Ni, Cu) when they become trapped at carbon vacancies in defective graphene. We have also considered the possibility that these vacancies become decorated by N atoms since it is found that there is a driving force for N dopants to migrate to the defect edges during preparation, forming pyridinic species.[26] Finally, we have studied the effect of the presence of a weakly/strongly interacting metal underlying substrates, i.e. Cu(111) and Ni(111).

First of all, we have learnt that carbon monovacancies are too small sites for TM trapping. The TM atoms do not well fit and they lie either above or below the graphene layer. On the contrary, carbon divacancies provide a hosting site of the proper size. The TM atom results to be coordinated either to four C atoms or to four N atoms (if the graphene is N-doped). The coordination is totally analogous to a square planar in molecular complexes. Here, the coordinating ligand is an infinite macrocycle made up by the graphene network surrounding the trapped TM atom. The TM d states become split according to a pseudo square planar geometry and then establish molecular orbitals with the sp_2 and p_z states of the coordinated C (or N) atoms from the surrounding graphene lattice. The d_{xy} and d_{z^2} are non-bonding orbitals, whereas $d_{x^2-y^2}$ forms σ bonds with sp_2 C (or N) states and d_{xz} and d_{yz} form π bonds with p_z C (or N) states. N 2p states are deeper than C ones, therefore the σ/σ^* pair also results to be deeper in energy when TM is coordinated to N atoms. The σ^* state is always found to be above the Fermi level, even if much less for the N-doped systems.

The presence of an underlying metal surface is to cause quenching of the residual magnetization on the metal center in most of the cases. Additionally, we observe that the d states with some z component mix up with the metal substrate band states becoming very broad. The non-bonding states remain very localized and can be used as reference states to understand modifications, shifts and trends along the period. There are not big differences between systems supported on Cu(111) or on Ni(111), except that on Ni we observe a slightly higher degree of mixing.

The Cu d states are very deep, with the σ^* state just above the Fermi level in the free-standing N-doped system. When a metal substrate is present underneath, electron charge is donated to the TM-graphene layer and even the σ^* state becomes partly occupied. However, Fe and Co d states, especially those not involved in x,y plane interactions with graphene are closer to the Fermi level and, therefore, lend themselves as potentially active sites for (single atom) catalysis.

From the energetics analysis, we have gained a lot of information on the relative role played by the different types of interactions (TM-G, TM-M(111), G-M(111)) in the balance between energy gain and energy loss. The main conclusion is that the Cu(111) substrate, being a weakly interacting support for the pristine graphene, is a more sensitive substrate to different chemically modified graphene layers (defective, with or without N, different TM trapped in the defects, etc.) than the Ni(111), which being strongly interacting, basically attracts anything which is laid over it. The cost of deformation or distortion is mostly paid by the graphene layer, especially when it is not N-doped. We have also learnt that SAC atoms mostly interact with the defective graphene and much less with the underlying substrate, even when the substrate is Ni(111), which keeps the graphene layer more tight and close to the surface. Finally, the energy decomposition analysis has highlighted that Cu is the least stable trapped metal atoms among those considered in this study, with the systematically lowest gain in the interactions, adsorption and binding.

Regarding HER, N-doping has improved the Gibb's free energy values only for Fe@4N2VG and Co@4N2G, with respect to the undoped cases, but worsened in all the rest of the cases. The interaction with the substrate improves the activity for the undoped cases and worsens for the N-doped cases. The best catalysts are Co@4N2VG and Co@2VG/Ni(111) among the systems studied here.

Supplementary Material

Graphene PDOS when adsorbed on Cu(111) and Ni(111), Optimized structures of free-standing undoped and N-doped 1VG and 2VG, 1VG and 2VG supported on Cu(111) and Ni(111), N-doped 1VG and 2VG supported on Cu(111) and Ni(111), Energy cost for TM to go through free-standing TM@1VG, Löwdin charges, Energy cost for Cu atom to pass from the up configuration through the C monovacancy to the down configuration for Cu@1VG/Ni(111) in fcc position with Ni(111) substrate, Optimized geometries of HER studies.

Acknowledgement

We are grateful to Cristina Africh and Daniele Perilli for useful discussions. This work has been supported by the project "MADAM - Metal Activated 2D cArbon-based platforMs" funded by the MIUR Progetti di Ricerca di Rilevante Interesse Nazionale (PRIN) Bando 2017 - grant 2017NYPHN8.

References

(1) S. Bohm, Graphene against corrosion. Nat. Nanotech. 2014, 9, 741-742.

(2) D. Prasai, J. C. Tuberquia, R. R. Harl, G. K. Jennings, K. I. Bolotin, Graphene: Corrosion-Inhibiting Coating. ACS Nano 6 (2012) 1102-1108. https://doi.org/10.1021/nn203507y.

(3) P. Z. Sun, Q. Yang, W. J. Kuang, Y. V. Stebunov, W. Q. Xiong, J. Yu, R. R. Nair, M. I. Katsnelson, S. J. Yuan, I. V. Grigorieva, M. Lozada-Hidalgo, F. C. Wang, A. K. Geim, Limits on gas impermeability of graphene. Nature 579 (2020) 229-232. https://doi.org/10.1038/s41586-020-2070-x.

(4) L. Tang, X. Meng, D. Deng, X. Bao, Confinement Catalysis with 2D Materials for Energy Conversion. Adv. Mater 31 (2019) 1901996. https://doi.org/10.1002/adma.201901996.

(5) K. S. Aneja, Bohm, H. M.; Khanna, A.; Bohm, S. Functionalised graphene as a barrier against corrosion. FlatChem 1 (2017) 11-19. http://dx.doi.org/10.1016/j.flatc.2016.08.003.

(6) S. Chen, L. Brown, M. Levendorf, W. Cai, S.-Y. Ju, J. Edgeworth, X. Li, C. W. Magnuson, A. Velamakanni, R. D. Piner, J. Kang, J. Park, R. S. Ruoff, Oxidation Resistance of Graphene-Coated Cu and Cu/Ni Alloy. ACS Nano 5 (2011) 1321-1327. https://doi.org/10.1021/nn103028d.

(7) R. K. S. Raman, P. C. Banerjee, D. E. Lobo, H. Gullapalli, M. Sumandasa, A. Kumar, L. Choudhary, R. Tkacz, P. M. Ajayan, M. Majumder, Protecting copper from electrochemical degradation by graphene coating. Carbon 50 (2012) 4040-4045. https://doi.org/10.1016/j.carbon.2012.04.048.

(8) N. T. Kirkland, T. Schiller, N. Medhekar, N. Birbilis, Exploring graphene as a corrosion protection barrier. Corrosion Science 56 (2012) 1-4. https://doi.org/10.1016/j.corsci.2011.12.003.

(9) M. Schriver, W. Regan, W. J. Gannett, A. M. Zaniewski, M. F. Crommie, A. Zettl, Graphene as a Long-Term Metal Oxidation Barrier: Worse Than Nothing. ACS Nano 7 (2013) 5763-5768. https://doi.org/10.1021/nn4014356.

(10) D. A. C. Brownson, S. A. Varey, F. Hussain, S. J. Haigh, C. E. Banks, Electrochemical properties of CVD grown pristine graphene: monolayer- vs. quasi-graphene. Nanoscale 6 (2014) 1607-1621. https://doi.org/10.1039/c3nr05643k.

(11) G. Giovannetti, P. A. Khomyakov, G. Brocks, V. M. Karpan, J. van den Brink, P. J. Kelly, Doping Graphene with Metal Contacts. Phys. Rev. Lett. 101 (2008) 026803. https://doi.org/10.1103/PhysRevLett.101.026803.

(12) X. Li, W. Cai, J. An, S. Kim, J. Nah, D. Yang, R. Piner, A. Velamakanni, I. Jung, E. Tutuc, S. K. Banerjee, L. Colombo, R. S. Ruoff, Large-Area Synthesis of High-Quality and Uniform Graphene Films on Copper Foils. Science 324 (2009) 1312-1314. https://doi.org/10.1126/science.1171245.

(13) F. Liu, D. F. Xue, Electrochemical energy storage applications of “pristine" graphene produced by non-oxidative routes. Sci. China Technol. Sci. 58 (2015) 1841-1850. https://doi.org/10.1007/s11431-015-5932-y.

(14) X. Wang, G. Sun, P. Routh, D.-H. Kim, W. Huang, P. Chen, Heteroatom-doped graphene materials: syntheses, properties and applications. Chem. Soc. Rev. 43 (2014) 7067-7098. https://doi.org/10.1039/c4cs00141a.

(15) Y. Wang, J. Mao, X. Meng, L. Yu, D. Deng, X. Bao, Catalysis with Two-Dimensional Materials Confining Single Atoms: Concept, Design, and Applications. Chem. Rev. 119 (2019) 1806-1854. https://doi.org/10.1021/acs.chemrev.8b00501.

(16) L. Zhang, Y. Jia, G. Gao, X. Yan, N. Chen, J. Chen, M. T. Soo, B. Wood, D. Yang, A. Du, X. Yao, Graphene Defects Trap Atomic Ni Species for Hydrogen and Oxygen Evolution Reactions. Chem 4 (2018) 285-297. https://doi.org/10.1016/j.chempr.2017.12.005.

(17) V. Carnevali, L. L. Patera, G. Prandini, M. Jugovac, S. Modesti, G. Comelli, M. Peressi, C. Africh, Doping of epitaxial graphene by direct incorporation of nickel adatoms. Nanoscale 11 (2019) 10358-10364. https://doi.org/10.1016/10.1039/c9nr01072f.

(18) L. L. Patera, F. Bianchini, C. Africh, C. Dri, G. Soldano, M. M. Mariscal, M. Peressi, G. Comelli, Real-time imaging of adatom-promoted graphene growth on nickel. Science 359 (2018) 1243-1246. https://doi.org/10.1126/science.aan8782.

(19) D. Deng, X. Chen, L. Yu, X. Wu, Q. Liu, Y. Liu, H. Yang, H. Tian, Y. Hu, P. Du, R. Si, J. Wang, X. Cui, H. Li, J. Xiao, T. Xu, J. Deng, F. Yang, P. N. Duchesne, P. Zhang, J. Zhou, L. Sun, J. Li, X. Pan, X. Bao. 2015. A single iron site confined in a graphene matrix for the catalytic oxidation of benzene at room temperature. Sci. Adv. 11, e1500462. https://doi.org/10.1126/sciadv.1500462.

(20) H. Fei, J. Dong, M. J. Arellano-Jimenez, G. Ye, N. D. Kim, E. L. G. Samuel, Z. Peng, Z. Zhu, F. Qin, J. Bao, M. J. Yacaman, P. M. Ajayan, D. Chen, J. M. Tour, Atomic cobalt on nitrogen-doped graphene for hydrogen generation. Nat. Commun. 6 (2015) 8668. https://doi.org/10.1038/ncomms9668.

(21) Y. Shao, S. Zhang, M. H. Engelhard, G. Li, G. Shao, Y. Wang, J. Liu, I. A. Aksay, Y. Lin, Nitrogen-doped graphene and its electrochemical applications. J. Mater. Chem. 2010, 20, 7491-7496. https://doi.org/10.1039/c0jm00782j.

(22) Y. Wang, Y. Shao, D. W. Matson, J. Li, Y. Lin, Nitrogen-Doped Graphene and Its Application in Electrochemical Biosensing. ACS Nano 4 (2010) 1790-1798. https://doi.org/10.1021/nn100315s.

(23) H. Xu, L. Ma, Z. Jin, Nitrogen-doped graphene: Synthesis, characterizations and energy applications. J. Energy Chem. 27 (2018) 146-160. https://doi.org/10.1016/j.jechem.2017.12.006.

(24) H. Wang, T. Maiyalagan, X. Wang, Review on Recent Progress in Nitrogen-Doped Graphene: Synthesis, Characterization, and Its Potential Applications. ACS Catal. 2 (2012) 781-794. https://doi.org/10.1021/cs200652y.

(25) H. M. Jeong, J. W. Lee, W. H. Shin, Y. J. Choi, H. J. Shin, J. K. Kang, J. W. Choi, Nitrogen-Doped Graphene for High-Performance Ultracapacitors and the Importance of Nitrogen-Doped Sites at Basal Planes. Nano Lett. 11 (2011) 2472-2477. https://doi.org/10.1021/nl2009058.

(26) S. Fiori, D. Perilli, M. Panighel, C. Cepek, A. Ugolotti, A. Sala, H. Liu, G. Comelli, C.D. Valentin, C. Africh, “Inside out” growth method for high-quality nitrogen-doped graphene, Carbon, 171 (2021) 704-710. https://doi.org/10.1016/j.carbon.2020.09.056.

(27) P. Giannozzi, S. Baroni, N. Bonini, M. Calandra, R. Car, C. Cavazzoni, D. Ceresoli, G. L. Chiarotti, M. Cococcioni, I. Dabo, et. al. QUANTUM ESPRESSO: a modular and open-source software project for quantum simulations of materials. J. Phys.: Condens. Matter, 21 (2009) 395502. https://doi.org/10.1088/0953-8984/21/39/395502.

(28) H. J. Monkhorst, J. D. Pack, Special points for Brillouin-zone integrations. Phys. Rev. B 13 (1976) 5188-5192. https://doi.org/10.1103/PhysRevB.13.5188.

(29) T. Thonhauser, V. R. Cooper, S. Li, A. Puzder, P. Hyldgaard, D. C. Langreth, Van der Waals density functional: Self-consistent potential and the nature of the van der Waals bond. Phys. Rev. B 76 (2007) 125112. https://doi.org/10.1103/PhysRevB.76.125112.

(30) D. C. Langreth, B. I. Lundqvist, S. D. Chakarova-Käck, V. R. Cooper, M. Dion, P. Hyldgaard, A. Kelkkanen, J. Kleis, L. Kong, S. Li, A density functional for sparse matter. J Phys.: Condens. Matter 21 (2009) 084203. https://doi.org/10.1088/0953-8984/21/8/084203.

(31) T. Thonhauser, S. Zuluaga, C. A. Arter, K. Berland, E. Schröder, P. Hyldgaard, Spin Signature of Nonlocal Correlation Binding in Metal-Organic Frameworks. Phys. Rev. Lett. 115 (2015) 136402. https://doi.org/10.1103/PhysRevLett.115.136402.

(32) K. Berland, V. R. Cooper, K. Lee, E. Schröder, T. Thonhauser, P. Hyldgaard and B. I. Lundqvist, van der Waals forces in density functional theory: a review of the vdW-DF method. Rep. Prog. Phys. 78 (2015) 066501. https://doi.org/10.1088/0034-4885/78/6/066501.

(33) A. Kokalj, XCrysDen—a new program for displaying crystalline structures and electron densities. J. Mol. Graph. Model. 17 (1999) 176-179. https://doi.org/10.1016/s1093-3263(99)00028-5.

(34) J. K. Nørskov, T.Bligaard, A. Logadottir, J. R. Kitchin, J. G. Chen, S. Pandelov, U. Stimming, Trends in the exchange current for Hydrogen Evolution. J. Electrochem. Soc. 152 (2005) J23-J26. https://doi.org/10.1149/1.1856988.

(35) E. Skúlason, V. Tripkovic, M. E. Björketun, S. Gudmundsdóttir, G. Karlberg, J. Rossmeisl, T. Bligaard, H. Jónsson, J. K. Nørskov, Modeling the Electrochemical Hydrogen Oxidation and Evolution Reactions on the Basis of Density Functional Theory Calculations. J. Phys. Chem. C 114 (2010) 18182-18197. https://doi.org/10.1021/jp1048887.

(36) L. Adamska, R. Addou, M. Batzill, I. I. Oleynik, Atomic and electronic structure of graphene/Sn-Ni(111) and graphene/Sn-Cu(111) surface alloy interfaces. Appl. Phys. Lett. 101 (2012) 051602. https://doi.org/10.1063/1.4739475.

(37) W. Zhao, S. M. Kozlov, O. Hofert, K. Gotterbarm, M. P. A. Lorenz, F. Viñes, C. Papp, A. Gorling, H.-P. Steinruck, Graphene on Ni(111): Coexistence of Different Surface Structures. J. Phys. Chem. Lett. 2 (2011) 759-764. https://doi.org/10.1021/jz200043p.

(38) A. V. Krasheninnikov, P. O. Lehtinen, A. S. Foster, P. Pyykkö, R. M. Nieminen, Embedding Transition-Metal Atoms in Graphene: Structure, Bonding, and Magnetism. Phys. Rev. Lett. 102 (2009) 126807. https://doi.org/10.1103/PhysRevLett.102.126807.

(39) Y. Tang, J. Zhou, Z. Shen, W. Chen, C. Li, X. Dai, High catalytic activity for CO oxidation on single Fe atom stabilized in graphene vacancies. RSC Adv. 6 (2016) 93985. https://doi.org/10.1039/c6ra14476d.

(40) L. Wu, S. Hu, W. Yu, S. Shen, T. Li, Stabilizing mechanism of single-atom catalysts on defective carbon surface. Npj Comput. Mater. (2020) 6:23. https://doi.org/10.1038/s41524-020-0292-y.

(41) L. Wang, X. Zhang, H. L. W. Chan, F. Yan, F. Ding, Formation and Healing of Vacancies in Graphene Chemical Vapor Deposition (CVD) Growth. J. Am. Chem. Soc. 135 (2013) 4476−4482. https://doi.org/10.1021/ja312687a.